Spring 2014

Investigation of fluids flow behavior in nano-scale channels by using optic imaging system

Qihua Wu

Recommended Citation

Wu, Qihua, "Investigation of fluids flow behavior in nano-scale channels by using optic imaging system" (2014). *Doctoral Dissertations*. 2197.
https://scholarsmine.mst.edu/doctoral_dissertations/2197

INVESTIGATION OF FLUIDS FLOW BEHAVIOR IN NANO-SCALE CHANNELS

BY USING OPTIC IMAGING SYSTEM

by

QIHUA WU

A DISSERTATION

Presented to the Faculty of the Graduate School of the

MISSOURI UNIVERSITY OF SCIENCE AND TECHNOLOGY

In Partial Fulfillment of the Requirements for the Degree

DOCTOR OF PHILOSOPHY

in

CHEMISTRY

2014

Approved by

Dr. Yinfa Ma, Advisor

Dr. Baojun Bai, Co-advisor

Dr. Klaus Woelk

Dr. Paul Nam

Dr. Jeffrey G. Winiarz

PUBLICATION DISSERTATION OPTION

This dissertation consists of the following three articles that have been published, submitted for publication, or will be submitted for publication. Pages 13 – 29 were published in LAB ON A CHIP. Pages 30 – 58 were accepted to publish in to SPE JOURNAL. Pages 59 – 77 were under preparation and will be submitted to LAB ON A CHIP.

ABSTRACT

Tight gas and shale gas reservoirs are characterized to have small pores with diameters in nanometer (nm) range. The physics of fluid flow in nanopores is poorly understood. Knowing the fluid flow behavior in the nano-range channels is of major importance for stimulation design, gas production optimization and calculations of the relative permeability of gas in tight shale gas systems. In this work, a lab-on-chip approach for direct visualization of the fluid flow behavior in nano-scale channels was developed using an advanced epi-fluorescence microscopy method combined with a nano-fluidic chip. The nanofluidic chips with different dimensions were designed and fabricated. First a concentration dependent fluorescence signal correlation was developed for the determination of single phase flow rate. Experiments of water/gas flow in nano-scale channels with 100nm depth were conducted. Meanwhile, three different flow patterns were observed from two phase flow in nano-scale channels experiments and their special features were described. The displacements of two-phase flow in 100 nm depth slit-like channels were reported in the second part of this work. Specifically, the two-phase gas slippage factor as the function of water saturation was studied. Moreover, water/gas two phase displacements were visualized in nanochanels with various depths. The displacements mechanisms for both drainage and imbibition processes were discussed and water/gas relative permeability in nano-scale channels were summarized. The residue water/gas saturations in nano-scale channels were also characterized. The results of this work are crucial for permeability measurement and understanding fluid flow behavior for unconventional shale gas systems with nanopores.

ACKNOWLEDGMENTS

I would like to acknowledge the contribution to this work of a number of people, whose support and assistance played a key role in my research in the past years.

I would like to express my gratitude and respect to my advisor, Dr. Yinfa Ma. He made sure that I learned not only the fundamental knowledge, also experimental skills, logical thinking and problem solving abilities during my Ph.D. studies. His direction in all aspects of my graduate work was invaluable and will be forever appreciated.

I would like to express my gratitude to my co-advisor, Dr. Baojun Bai. We had regular weekly meetings with presentations on research progress and he was always there to discuss the problems and difficulties with me and pose new research ideas. I would also like to thank my graduate committee members, Dr. Klaus Woelk, Dr. Paul Nam and Dr. Jeffrey G. Winiarz, for the various ways in which they assisted me in my Ph. D study.

The work was supported by Dr. Baojun Bai and Dr. Yinfa Ma's fund from Research Partnership to Secure Energy for America (RPSEA). I am thankful for their financial support.

I would like to thank all my group members who were constantly helping and supporting me.

Finally, I would like to thank my family, especially my parents and my wife, for their untiring support and encouragement. I thank my two-year old daughter for love and joy she brought to my life. Love from family will always be strength to me.

TABLE OF CONTENTS

SECTION

LIST OF ILLUSTRATIONS

LIST OF TABLES

SECTION

1. INTRODUCTION

1.1 BACKGROUND

Unconventional gas has become an important energy resource that mainly developed in North America and prospected for globally. Unconventional gas plays are the natural gas reservoirs that needs to be produced or extracted using techniques other than the conventional method. In the United States, coal-bed methane, shale gas, and tight (low-permeability) gas plays were primarily considered as unconventional. As the conventional gas resources are easily produced and more exploited, unconventional gas resources are becoming a larger contributor to annual gas production in the United States. For example, unconventional shale gas has accounted for more than 14% of produced gas in the United States by the end of 2004 (Energy Information Administration [EIA], 2004). Recently, the USGS estimated that low permeability tight-sands and gas shale in the U.S. may hold up to 626Tcf (Trillions of cubic feet) of gas (USGS, 2013/3/13). There are about 200,000 unconventional gas wells in low permeability sands, coal-bed methane deposits, and gas shale in the lower-48 states.

The unconventional gas reservoirs, such as tight sand and shale gas have micro-Darcy (μD) or even nano-Darcy (nD) range permeability. They are characterized with pore sizes and pore throat radius in the range from 1 to 300 nanometers, which are much smaller compared with conventional sandstone and carbonate reservoirs with pore sizes in the range of 1 to 100 micrometers [1]. These properties result in some characteristic

features such as high capillary pressure, low porosities, and high wetting phase residue saturation. In order to produce or extract natural gas from these extremely low permeability gas reservoirs, different types of fluids, such as water, surfactant solutions or polymer solutions are normally introduced into the formations during the hydraulic fracturing stimulation, drilling and completion processes [2]. Currently, the selection of hydraulic fracturing fluids and design of production for unconventional gas reservoirs are based on conventional oil & gas techniques and practices. However, the fluids transportation mechanisms are not well understood in the nanopores in shale and tight sand formations. In addition to conventional viscous flow, other transportation mechanisms may occur. Thus, understand the fluids flow behavior will essential for design of the hydraulic fracturing, drilling and completion.

1.2 THEORY

1.2.1 Permeability and Darcy's Law. For a porous media, the ability to conduct fluids flow is termed as permeability. In the shale gas reservoirs, rocks are considered as porous media. The permeability of a rock depends on effective porosity, grain shape, grain size distributions, materials of grains. For fluids flow in porous media, Darcy's law is one of the standard mathematical tools in the field of petroleum engineering, which is an empirical formula based on results of experiments on the flow of water through beds of sand, established by Henry Darcy in 1856. The Darcy's equation is expressed in differential formats follows:

$$Q = \frac{-kA}{\mu} \frac{(P_a - P_b)}{L} \qquad\qquad Eq.1$$

Where:

Q - fluid flow rate, cm^3/s

K – permeability of the porous media, Darcy

A – cross section area, cm^2

$\boldsymbol{\mu}$ - viscosity of the fluid, cetipoises (cP)

L – length of the porous media, cm

P_a – inlet pressure, atm

P_b – outlet pressure, atm

Darcy's law assumes that the flow is driving by viscous pressure and the gravitational force. And it also assumed that the flow rate is linearly proportional to the driving force. For single phase flow, the permeability, k, from Darcy's equation is termed as the "absolute" permeability when the rock is considered to be saturated with just single fluid (water, gas or oil). For multiphase flow, whereas the rock is saturated by more than one type of fluids, the permeability of each phase (or fluid) is termed as "effective" permeability. The flow rate of each phase is still considered to be linearly proportional to the driving force as in single phase, but the proportionality coefficient should depend on fluid saturation in the rocks. Under those conditions, the ratio of effective permeability of one phase to the absolute permeability of the rock is known as the "relative" permeability (k_r) of that phase.

Although Darcy's law was determined experimentally by Darcy, it has since been derived from the Navier-Stokes equations followed the classic viscous flow theory. In the classic viscous flow mechanics, the continuum theory assumes that fluids velocity is zero at the pore wall. For conventional gas reservoirs with pore radius in the range of 1 to 100

micrometer, this assumption is considered valid since the fluid flows as continuous medium. And Darcy' law has been used for modeling of the pressure-driven viscous flow in these reservoirs.

1.2.2 Capillary Pressure. Darcy's law assumes that the fluids flow is only driven by the pressure. In the presence of multiphase, the equilibrated pressure difference between two phases (or immiscible fluids) across their interfaces is termed as "capillary pressure". If two immiscible fluids are in contact with a capillary, one fluid is always intend to "wet" the capillary walls over the other fluid and thus to form a curvature interface. The fluid that intends to wet the capillary walls is considered as the wetting fluid (or phase) and the other fluid is non-wetting fluid (or phase). Thus the capillary pressure is defined as the pressure difference between the non-wetting and wetting fluids (or phases):

$$\mathbf{P_c = P_n - \ P_{nw}} \qquad\qquad \text{Eq.2}$$

Where P_c is the capillary pressure, P_{nw} is the pressure of non-wetting fluid and P_w is the pressure of wetting fluid.

For a capillary with uniform surface property and radius, the capillary pressure can be calculated from the equation:

$$\mathbf{P_c} = \frac{2\sigma cos\theta}{R} \qquad\qquad \text{Eq. 3}$$

Where $\boldsymbol{\sigma}$ is the interfacial tension; $\boldsymbol{\theta}$ is the static contact angle and R is the pore radius.

For multiphase flow in the porous media, another central theory is that capillary pressure is function of phase saturation, which can be defined by the equation:

$$P_n - P_{nw} = P_c(S_w) \qquad \text{Eq. 4}$$

Where S_w is the wetting phase saturation. However, for the above equation, there is not a unique correlation between capillary pressure and wetting phase saturation. The correlation largely depends on the geometry of the porous media and two phase saturation distribution. Most capillary pressure − saturation relationships were obtained from experimental data in micro-scale pores and no independent models were derived. For nanopores, there is very few of results of correlation between the capillary pressure and the saturation.

1.2.3 Klinkenberg Theory. When we consider the gas flow in nanopores, the mean free path of the gas molecule (0.4nm) is only one or two magnitude smaller than the flow diameter. At this dimension, the continuum flow theory may break down since the contribution of gas molecule free movement to the flow is not negligible. Moreover, when gas molecules strike against the pore wall, they tend to keep moving (or so called "gas slip"), so the velocity will not be zero at the pore walls. Under such conditions, the gas flow rate calculated by the standard Darcy's law may have significant deviations from the true value.

The gas slip flow was first studied by Klinkenberg [3], and the Klinkenberg equation is expressed as follows:

$$k_g = k_{g\infty} \cdot (1 + \frac{4c\lambda}{r}) \qquad \text{Eq. 5}$$

Where k_g is the apparent gas permeability at a mean pressure, p_m;

$p_m = \dfrac{(p_i + p_o)}{2}$; p_i and p_o are inlet and outlet pressures of the test section, respectively.

$k_{g\infty}$ is the intrinsic permeability of gas at infinite pressure, λ is the mean free path of the gas molecule; r is the radius of the pore; and c is a constant.

Klinkenberg reduced Eq. 5 to:

$$k_g = k_{g\infty} \cdot (1 + \frac{b}{p_m}) \qquad \text{Eq.6}$$

Where b is the gas slippage factor, which is defined as:

$$b = \frac{4c\lambda p_m}{r} = \frac{4c'}{r} \qquad \text{Eq.7}$$

The mean free path of the gas is inversely proportional to the mean pressure, p_m, so the factor c' represents a constant at a certain mean pressure.

Klinkenberg theory is a practical approach for petroleum engineering but it is assuming that the gas is flowing at very low pressures based on the Darcy's law. Other flow mechanism, such as mass diffusions on the total flux was not considered in Klinkenberg theory.

1.3 USING MICROFLUIDIC CHIP FOR FLUID FLOW STUDIES

Over the last several decades, microfluidic devices have been increasingly used to study fluids flow behavior in various research areas including chemical, chemical

engineering, biomedical and physical applications. Microfluidic devices have been demonstrated to be a valuable tool for the studies of fluid flow in porous media since it enables the real-time visualization. With the advance of techniques, the fabrication of nanofluidic devices with nanopores becomes feasible. This section will briefly review the previous works of studying fluids flow behavior in micro-scale and nanopores.

1.3.1 Visualization of Fluids Flow Behavior in Micro-models. Fluids flow behavior, especially the two-phase displacements in the micro-scale pores have been extensively studied by using the microfluidic chips [4-23].

For most of these works, soft lithography or deep reactive ion etching techniques have been used to fabricate the micro-models. Glass or quartz has been the major choices of the materials of micro-models, while PDMS is also used in some cases.

Lenormand et al., [14] studied mechanisms of the two-phase displacements in an etched transparent polyester resin micro-model with network patterns. Both imbibitions and drainage processes were performed and the results of pressure and saturation were compared with calculated values. Different two-phase displacement patterns were also observed under different conditions. Feng et al., [11] studied three phase displacements in glass network micro-models. Water-alternating gas (WAG) displacements were performed in the network micro-models which has the similar patterns as the target reservoir rock. The results show that the mechanism of WAG flow in porous media is much different from two phase (gas-oil and water-oil) flow. Flow patterns during the displacement are largely dependent on the pore sizes and pore geometry. Chang et al. [7] conducted two-phase displacement experiments following Lenormand's assumptions [14]. They found that the displacement mechanisms in imbibitions are mainly snap-off and

piston-type motion. Their experiment results provided valuable experimental support and suggestions for Lenormand's displacement assumptions, which are the basis for many related experimental and numerical studies. Dawe et al., [21] performed immiscible displacements of two phases in heterogeneous micro-models. The permeability was controlled by packing unconsolidated glass bead packs. The results demonstrated the strong effect of heterogeneities on the displacement patterns as well as the phase saturations.

1.3.2 Measurements of Phase Saturation and Relative Permeability. Besides of the flow patterns and displacements mechanisms, the phase saturation can also be characterized from the visualization of fluids flow in micro-models. In general the phase saturation is determined by analyzing the area of the each phase over the total pore area at the 2D dimension (the x-y plane). This method is based on the assumption that the saturation over the z – depth is uniform. Recently, with the advance of confocal microscopy, 3D phase saturation measurement is becoming available.

The other parameters, such as capillary pressure and relative permeability at different phase saturations are also important since they are the bridge between the microscopic flow dynamics (flow patterns and mechanisms) and the macroscopic behavior (phase saturation) in the porous media. In order to measure the relative permeability, phase pressure and flow rate need to be accurately measured and controlled and in corporate with the phase saturation data.

Tsakiroglou et al. [18] studied the immiscible two-phase displacements of shear thinning fluids in micro-models. They have found that at various capillary numbers, the flow pattern and the relative permeabilities of the two phases are different.

Theodoropoulou et al., [15] performed visualization experiments of the unsteady immiscible two-phase displacement on glass-etched pore networks. Fluids were pressure-injected into the network at a fixed flow rate with the use of a syringe pump. The processes of displacement at the central region of the network were captured by the CCD camera. The pressure drop along the test region was measured by a pressure transducer, with respect to time. This procedure allowed the determination of saturation and relative permeability of each phase as a function of time. The relative permeability and capillary pressure curves were estimated from transient displacement experiments. The results have shown that the relative permeability and capillary pressures are not unique functions of the fluid saturation, but also closely related to the capillary number and flow patterns. These results are agreed with results obtained by Tsakiroglou et al.[18]. They have also found that for imbibitions, capillary pressure is a decreasing function of capillary number which is in agreement with the linear thermodynamic theory. Sohrabi et al., [24] studied the oil recoveries after WAG processes in glass network micro-models. The oil saturation and recoveries after WAG injection were obtained based on the imaging data. Their results showed that, under all tested wettability conditions, oil recovery by alternating injection of WAG was higher than water or gas injection alone. Recently, Karadimitriou et al., [13] visualized and recorded the distribution of fluids throughout the micro-model. Quasi-static drainage experiments were conducted in order to obtain equilibrium data points. By measuring the flow rate of liquid through the flow network for known pressure gradients, the intrinsic permeability of the micro-model was also calculated.

Although numerous works have been done for the fluid flow in micro-scale pores by using microfluidic devices, the measurement of relative permeability and capillary

pressures are still challenging. In the complex flow networks with very small dimensions, it is very difficult to control and measure local pressure and flow rate.

1.3.3 Visualization of Fluids Flow in Nanopores. Although fluids flow in micro-scale pores have been extensively studied, there are still lots of unknown questions for fluids flow in nanopores. The major challenges of studying fluids flow in nanopores are (1) visualization of fluids under nano-scale and (2) accurately control/measure fluid flow pressure and flow rate. In order to overcome the sensitivity issue of the image, fluorescent dye is added into the fluids and epi-flurescence microscopy method is normally used. For the second problem, generally a large number of nanopores or channels were fabricated and the bulk pressure or bulk flow rate is monitored by the pressure transducer/flow meter. Thus the obtained pressure and flow rate data for fluid flow in nanopores only represents the average value. In real reservoir rock, which always has the heterogeneous pore structure, the average results are clearly not enough for the understanding of fluids flow.

Most published studies for fluid flow in nanopores are under extreme simple conditions - nanopores are mostly straight channel or nanotubes [25-38]. At the nanopores scale, Darcy's law is not practicable anymore and Knudsen diffusion model was generally used.

Cooper et al., [26] have measured the mass transport of different gases through a carbon nanotube-based membrane and nanoporous alumina with 200 nm pore dimensions. It was found that the gas flow through the nanoporous alumina membrane is consistent with Knudsen-type diffusion. However, the permeability relationships in the carbon nanotube-based membrane present different trends which the diffusion rates are strongly

dependent on pressures. The proposed mechanism for this behavior is the elastic deformation of the membrane that causes the flow between the nanotubes.

Holt et al., [30] have reported the measurements of gas and water mass transports through membranes that consisted of carbon nanotubes with diameters of less than 2 nanometers serve as pores. The measured gas flux through the carbon nanotube-based membranes exceeded the flux predicted by Knudsen diffusion model by at least one or two order of magnitude. The measured permeability relationship of water flow is more than three orders of magnitude larger than that obtained from non-slip hydrodynamics model, but fits well with the results of Molecular Dynamic simulation.

1.4 RESEACH OBJECTIVES

This work aims to improve the understanding for the introduced fluid flow behavior in tight gas and shale formations by using advanced optic imaging system combined with nanofluidic chips. This is accomplished through the following specific objectives:

1. Developing an advanced optic imaging method for visualization of fluids flow in nanopores, by using the designed and fabricated nanofluidic chips.

2. Designing and materializing an experimental setup that allows control/measure pressure across the tested sections.

3. Designing and performing experiments of water/gas two-phase flow in fabricated nanofluidic chips.

4. Characterizing the phase saturation, capillary pressure, relative permeability and other parameters in the nanopores.

1.5 DISSERTATION ORGANIZATION

This dissertation is organized as follows.

In Paper I, a lab-on-chip technique for direct visualization of the single- and two-phase pressure driven flows in nano-scale channels was developed. The nanofluidic chip was designed and fabricated; concentration dependent fluorescence signal correlation was developed for the determination of flow rate. Experiments of single and two phase flow in nano-scale channels with 100nm depth were conducted. The linearity correlation between flow rate and pressure drop in nanochannels was obtained and fit closely into the Poiseuille's Law. Meanwhile, three different flow patterns, single, annular, and stratified were observed from two phase flow in nanochannels experiments and their special features were described. Two-phase flow regime map for nanochannels was presented.

In Paper II, displacements of water/gas two-phase flow in 100 nm depth slit-like channels were investigated by the optic imaging method developed in Chapter 2. Specifically, the two-phase gas slip effect was investigated. Under experimental conditions, the gas slippage factor increased as the water saturation increased. The two-phase flow mechanism in one dimensional nano-scale slit-like channels was proposed and proved by the flow pattern images.

In Paper III, water/gas two phase displacements were studied in the nano pores with different dimensions and pore structures. The relationship between capillary pressures and phase saturations were obtained for both drainage and imbibitions

processes. The displacement mechanisms during imbibitions and drainage were discussed. The relative permeability as a function of wetting phase saturation for nanopores was also reported for the first time.

PAPER

1. Optic Imaging of Single and Two-Phase Pressure Driven Flows in Nano-Scale Channels

ABSTRACT

Microfluidic and nanofluidic devices have undergone rapid development in recent years. Functions integrated onto such devices provide lab-on-a-chip solutions for many biomedical, chemical, and engineering applications. In this paper, a lab-on-chip technique for direct visualization of the single- and two-phase pressure driven flows in nano-scale channels was developed. The nanofluidic chip was designed and fabricated; concentration dependent fluorescence signal correlation was developed for the determination of flow rate. Experiments of single and two phase flow in nano-scale channels with 100nm depth were conducted. The linearity correlation between flow rate and pressure drop in nanochannels was obtained and fit closely into the Poiseuille's Law. Meanwhile, three different flow patterns, single, annular, and stratified were observed from two phase flow in nanochannels experiments and their special features were described. Two-phase flow regime map for nanochannels was presented. Results are of critical importance to both fundamental study and many applications.

1. INTRODUCTION

Over the past decade, the field of microfluidics and nanofluidics has attracted significant research effort with the rapid development of micro/nano-devices fabrication technologies and fluid manipulation systems. Lab-on-a-Chip devices (LOC) and related research have wide range applications and availabilities in fields of biomedical, [39, 40] chemical synthesis, [41] chemical engineering [42] and petroleum refinery. [43] Therefore, the understanding of fluid flow behavior is crucial for both fundamental study and new technique development and application.

Three types of actuation principles are commonly applied in microfluidic devices: capillary pumping, mechanical pumping and non-mechanical pumping, such as electro-osmotic flow (EOF). There have been numerous publications related to capillary filling process of liquid/gas in the nano- and micro-channels, [27, 28, 33, 35, 36, 44, 45] or the EOF in nanochannels. However, applications of these two pumping methods are limited. For example, only aqueous solution can be utilized in EOF system. Pressure driven method by using mechanical pump is more favorable for the technical development in chemical processes, chemical engineering, petroleum engineering and many other fields. Pressure driven flow in mini and microchannels have been well studied and different models have been developed. [34, 46-50] Serizawa et al. [51] carried out visualized investigations on air-water two-phase flow in circular tubes with 20, 25, and 100 μm of inner diameter (i.d.) and steam-water flow in a 50 μm i.d. circular tube, with the superficial velocities covering a range $J_L = 0.003$ - 17.52 m/s and $J_G = 0.0012 - 295.3$ m/s. Some distinctive flow patterns were identified both in air–water and steam–water systems. It has been demonstrated that two-phase flow patterns are sensitive to the

surface conditions of the inner wall of the test tube. The comparison of the two-phase flow pattern map with the Mandhane's correlation showed that general trends in the microchannels follow the Mandhane's prediction. [52] As the channel dimension decreases, it was found that the properties of fluid flow in sub-micron and nanochannels are not only related to the local shear rate but also dependent on the channel dimensions. [25, 29, 34, 53] Travis et al. [53] reported that the classical Navier–Stokes behavior is approached for the channel width of about 10 folds of molecular diameters.

When the dimensions of channels decrease to nano-scale, there are limited study of single and two phase pressure driven flow due to some major technical challenges. First, traditional mechanical pumping method is hard to be applied for nanofluidic experiments due to the large hydrodynamic resistance and ultra-small volume of the nanochannels. It is very challenging to retain stable pressure and flow rate through the nanochannels by direct pumping. Therefore, indirect injection method has been developed and used by more researchers. [34, 54] The other challenge for the nanofluidic study is the measurement of fluid flow velocity/flow rate. Optic imaging method is commonly used for single and multi-phase flow rate measurement, since the images can provide real time velocities/flow rate and other important information – flow profile and residual layer thickness for example. To overcome the lack of sensitivity under small scales, most optic imaging methods use fluorescent tracers – either fluorescent particles or fluorescent molecules. [55-57] Compared to particle imaging velocimetry (PIV), molecules based method – molecular tagging velocimetry (MTV) [34] is much less intrusive and more suitable for the ultra-small scales of nanochannels due to the much smaller size of molecules compared to particles. Generally the displacement of tagged

region is measured and velocity profile is determined. Cuenca et al. [34, 54] developed an approach to determine the velocity by measuring the displacement of a fluorescence photo-bleaching line, which is relatively good below micron scale. For those methods, a complex optical system has to be constructed and aligned in order to perform accurate measurement.

In this study, a novel and comprehensive lab on chip approach was developed to investigate single/two-phase flow behavior in nano-scale channels. A concentration dependent fluorescence signal change correlation method has been developed for flow rate determination in LOC devices. Unique nanofluidic chips were designed and fabricated and the pressure drop of the nanochannels was controlled by an indirect method. The single and two phase flow behaviors in nanochannels were investigated by using these nanofluidic chips. The single phase flow rates versus the pressure drop across the nanochannels were first investigated, and the velocity and channel geometry effects on the two-phase flow patterns were then evaluated. The flow patterns and flow regime map in nanochannels were reported. This new method can also be used for many different types of LOC devices while avoiding the need of complex optical system.

2 EXPERIMENTAL METHODS

2.1 Materials and equipment

High purity nitrogen gas was used as the gas phase. Ultra-pure water was served as the liquid phase and pre-filtered by 0.22μm pore size Nylon filter before using. Alexa 488 (100mg/L) was purchased from Microprobe and used as the fluorescent dye in the liquid phase.

Two KD Scientific KDS 101 syringe pumps were used to generate the flow. All images were captured by a reverse microscope (Olympus, IX-51) and high-speed ICCD camera. The ICCD camera was operated at -20 ℃; the gain and exposure times were set at 150 and 100 ms, respectively. The delay of the shutter driver was set to 10 ms. Data were acquired through the Cellsens software provided by Olympus.

2.2 Nanofluidic chip design and fabrication

The schematic of nanofluidic chip is shown in Figure 1. In order to control the pressure difference across the nanochannels, two microchannels for fluid injection were connected to nanochannels. The lengths of the microchannels are equal in order to balance the pressure drops. T-shaped junctions were used to connect nanochannels with microchannels to avoid direct injection which may increase the chance of nanochannel clogging. A total of 100 parallel nanochannels were built between the microchannels to reduce the large hydrodynamic resistance.

Micro- and nanochannels of the nanofluidic chip were formed in double side polished <100> silicon wafers (thickness = 250 μm) with low-stress silicon nitride (~100 nm) on both sides using methods described in the literature.[32] First, an array of 100 nanochannels spaced 10 μm edge-to-edge were defined by reactive ion etching using photoresist and silicon nitride as etching mask on the front side of the wafer. Typical RMS horizontal surface roughness by reactive ion etching is known to be lower than 1 nm on 1 μm^2 zone.[38] Each channel had cross-sectional dimensions of 100 nm (depth) by 5 μm (width), and was 200 μm long. Next, two microchannels were defined on both sides of the nanochannel array. The microchannels had cross-section dimension of 10 μm

(depth) by 50 μm (width). Finally, inlet and outlet holes were defined at the four ends of the two microchannels by a back side deep reactive ion etching through the wafer. Fabricated device was removed from the wafer by cleavage along crystal planes. The front side of each device (40 mm x 20 mm x 0.25 mm) was anodically bonded (330 °C, 1 kV, 1 hr) to a thin Pyrex coverslip (Pyrex 7740, 40 mm x 20 mm x 0.3 mm, Newport Industrial Glass, Inc, Stanton, CA). Prior to the Si-Pyrex bonding, silicon nitride film was completely removed by hot phosphoric acid etching (85 wt% H_3PO_4, 2 hrs at 150 °C) procedure. In order to maintain a clean surface condition, the whole nanofluidic chip was rinsed by lab reagent water, methanol and dried by nitrogen gas prior to use.

2.3 Pressure driven flow across the nanochannels

Pressure-driven flow was established in the nanochannels by using the method developed in previous publications [34, 54] –controlling the pressure difference between the two microchannels. Experimental setup including pressure control system is shown in Figure 1. For the single phase flow, pressures P_1 and P_2 were controlled and applied to microchannels 1 and 2 by pressure regulators. Since the hydrodynamic resistance in nanochannels is much higher than that in microchannels, most of the injected fluids went through the microchannels. Thus, the contribution of flows in nanochannels to the flows in microchannels is negligible and stable pressure gradient and flow rate can be achieved in the microchannels. For a single nanochannel i, if its end pressures are named as P_{i1} and P_{i2}, the distance from the inlet to this nanochannel is L_i and the total length of each microchannel is L, the pressure drop Δp_i will be equal to $\frac{(P1-P2)(L-Li)}{L}$. Since the space of nanochannels array is very small (<1mm) comparing to the length of the microchannel

(45mm), and the nanochannel array connect to the center of the microchannel, the pressure difference across the nanochannels is nearly identical. Since $L_i \approx \frac{1}{2}L$, the pressure drop across the nanochannels is $\Delta p = \frac{P1-P2}{2}$. For the two phase flow in nanochannels, there were no well-developed methods for the control and velocity measurement. Based on the channel-structure, pressure drop was controlled and the velocities of two phases were measured indirectly. Gas and liquid phase were premixed and inlet pressure of the mixer was controlled by the pressure regulator. The average liquid flow rate was determined by the method used for single phase flow. The flow rate of gas phase was determined by measuring the size of formed gas bubble in microchannel 2, which served as batch collector. Then velocities of gas and liquid phase in nanochannels were calculated based on the flow rate divided by the volume of the nanochannel. Since the velocities were indirect measured and may have some deviations from the real velocities, the term "superficial velocity" was used instead.
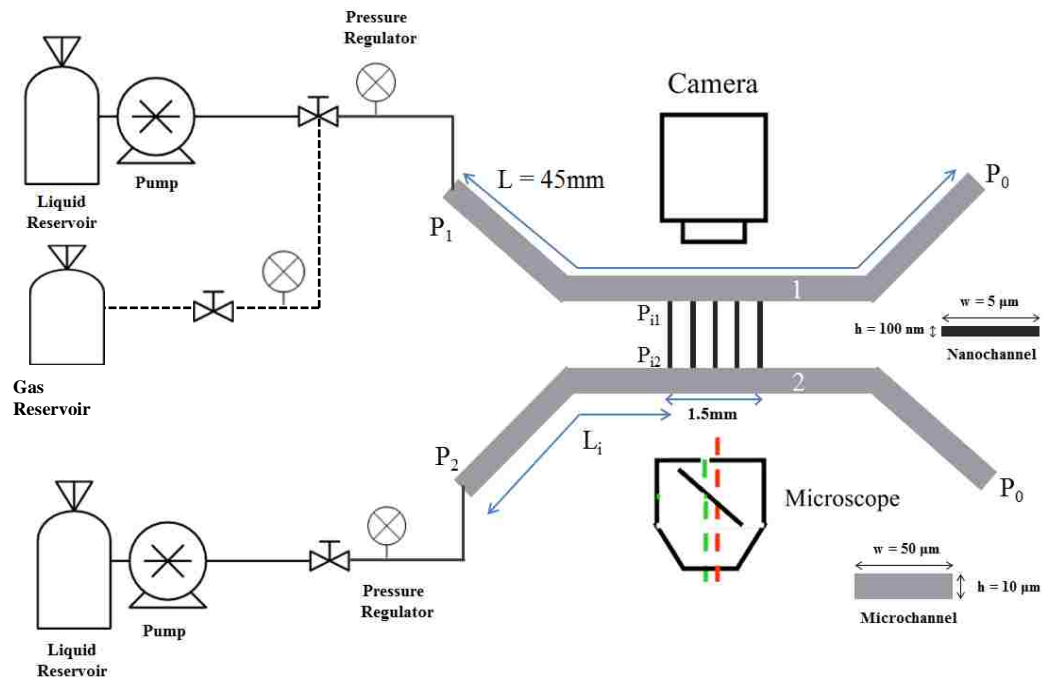
Figure 1.Fluid transport system and schematic of the nanofluidicchip. Solid lines are for liquid transportations and dotted line is for gas transportation in two-phase flow experiments. P_1 is inlet pressure on microchannel 1, P_2 is inlet pressure on microchannel 2; P_0 is outlet pressure for both microchannels; P_{i1} and P_{i2} are the end pressure of selected nanochannel; L is the total length of each microchannel, L_i is the distance from the microchannel inlet to connection of the selected nanochannel.

3. RESULTS AND DISCUSSION

3. 1 Flow rate determination of single phase flow in nanochannels

Unlike two phase flow, no interface can be used to monitor flow rate for a single-phase flow. Thus, it is not possible to determine flow rate by tracking the interface. As discussed in the Introduction, μPIV (particle imaging velocimetry) is also not viable due to the small size of the channels. MTV (molecular tagging velocimetry) and newly developed photo-bleaching velocimetry [54, 55] are commonly considered to be suitable

for the velocity measurement in nano-scale channels. However, there are still some limitations such as sensitivity and complex optic arrangement need to be improved. Thus, we developed a novel method to determine the flow rate in nanochannels which is to measure the concentration dependent fluorescence signal change based on the Beer Lambert's law. The principle of Beer Lambert's law has been widely used in the spectroscopic photo-detector such as UV/Vis detector to measure the concentration of organic compounds. Recently the correlation between the concentration and the fluorescence signal has been investigated to be used as fluorescence concentration detector in microfluidic devices.[58] The equation of Beer Lambert's law is given as:

$$\varepsilon lc = \ln\frac{P_0}{P_T},$$
<div align="right">Eq. 1</div>

Where P_0 is the intensity/power of the incident light, P_T is the intensity/power of the transmitted light, l is the length of light path, c is the concentration of the fluorescence dye and ε is the molar absorption coefficient under wavelength λ. The absorbed light intensity, P_A, could be expressed as:

$$P_A = P_0 - P_T = P_0(1 - e^{-\varepsilon lc}).$$
<div align="right">Eq. 2</div>

The emitted fluorescence light power will be proportional to absorbed light intensity and quantum yield of fluorescence dye (φ):

$$P_F \propto \varphi \cdot P_A \propto \varphi \cdot P_0(1 - e^{-\varepsilon lc})$$
<div align="right">Eq. 3</div>

By simplify the equation:

$$P_F = k'(1 - e^{-\varepsilon lc})$$
<div align="right">Eq. 4</div>

Where k' is lumped parameter that depends on input power, quantum yield of the fluorescence dye and the collection efficiency of the optic system.

Since the intensity of the emitted light is measured by an optical detector (camera), the responses of the camera and the background signals also need to be taking into consideration. The response of the ICCD camera is generally determined by the photocathode material used in the Image Intensifier and it is wavelength dependent. Since the same fluorescence dye is used, the responsiveness is considered to be a fixed number. The background signal is defined as the signal without addition of fluorescence dye, which is generally caused by the dark current of the optic detector or the light leaking in the optical system. [58] Both of them are related to the input power of the excitation light. In order to reduce the effect of background noise, input power is set to a fixed number and the background intensity is measured as I_b. Thus, the normalized signal intensity in the optical detector which contributed by the emitted light is calculated as:

$$I(c) = I_s - I_b \qquad \text{Eq. 5}$$

Where I_s is the collected signal intensity and I_b is the measured background intensity.

The normalized fluorescence signal as a function of dye concentration ranging from 10^{-9} mole/L to 10^{-5} mol/L was measured and the results are showing in Figure 2. The molar concentrations of fluorescence dye were x-axis and the intensity of fluorescence signals (signal-background)/background were Y-axis. Figure 2(a) shows the entire tested fluorescence concentration range and Figure 2(b) shows the enlarged part of the Figure 2(a) while the concentration of fluorescence dye is in the range from 10^{-8} mole/L to 10^{-6}

mole/L. It was found that experimental results fit very well into theoretical calculations in the concentration range from 10^{-8} mole/L to 10^{-6} mole/L. Deviation is observed when concentration is above 10^{-6} M, which indicates the decrease of quantum yield caused by aggregation of dye molecules or self-quenching effect. [59, 60] Thus, the concentration of fluorescence dye we used was below 10^{-5} M to guarantee the accuracy of the method.
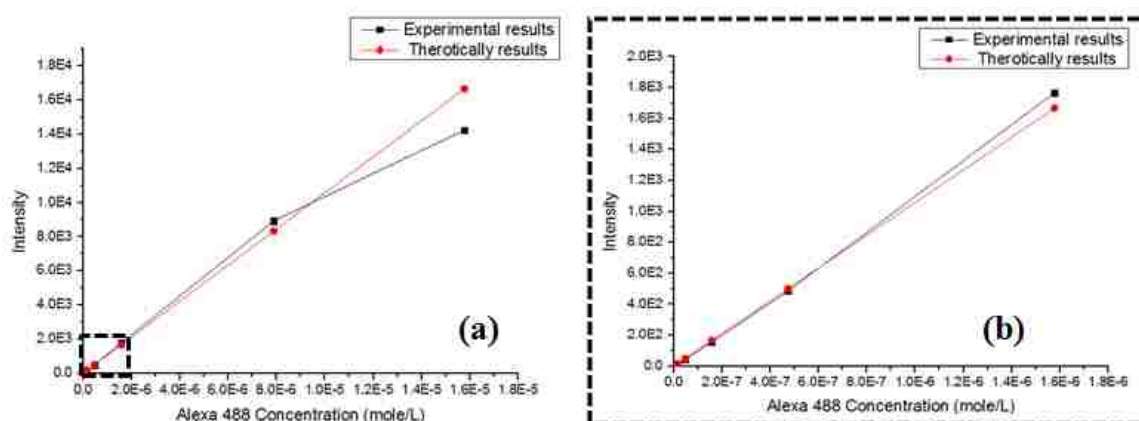
Figure 2.Comparisons between experiments results and theoretical results of intensity changes with different fluorescence dye concentration. (a). The whole range of concentration versus signal intensity; (b) Enlarged figure of low concentration range of fluorescence dye.

Back to Figure 1, stable pressure driven flow was established and microchannel 1 was served as the inlet channel. Microchannel 2 was served as the outlet and batch collector which both ends were connected to a small capped vial.

The concentration of fluorescence dye was maintained at C_1 in microchannel 1 while the initial concentration of dye in microchannel 2 was C_2 ($C_1 >> C_2$). While solution in microchannel 1transported into microchannel 2 through the nanochannels, the

concentration of dye in microchannel 2 would gradually increase to $C_2^{'}$ after certain time. Therefore, the average volume flow rate $\bar{q}$ in each single nanochannel could be obtained from:

$$\bar{q} = \frac{V(C_2^{'}-C_2)}{nt(C_1-C_2^{'})} \qquad \text{Eq. 6}$$

Where V is the volume of the microchannel, n is the total number of nanochannel, t is the time. Because the volume of the microchannel is much larger than the volume of nanochannels, all measurements were taken at least five minutes after the pressure was stable to ensure that the fluorescence signal in the microchannel 2 had significant change. Since this method is based on the mass transportation of the fluorescence molecules, the effect of diffusion need to be considered. The diffusion coefficient of the fluorescence dye – Alexa 488 in aqueous solution is 430 μm^2/s under room temperature (25 $^{\circ}$C). Under certain residence time, the average diffusion distance of the fluorescence dye is:

$$d = \sqrt{D \times t} \qquad \text{Eq. 7}$$

Where D is the diffusion coefficient of the molecule, t is the residence time. Under the experimental conditions, the residence time of the fluorescence dye in nanochannels is very small (0.1~0.3s). The average diffusion distance is calculated to be smaller than 10 μm, which is much smaller compare to the length of nanochannel (200 μm). Therefore, the contribution of the diffusion to mass transportation could be neglected.

By using this method, flow rate of single phase pressure driven flow through nanochannels under different pressure was measured and data is compared with

theoretical results obtained from Poiseuille's Law. The theoretical volume flow rate depends linearly on the pressure, which is integrated from Hagen–Poiseuille's equation [61] and the average flow rate q in nanochannel is given by:

$$q = \frac{\Delta P}{l} \frac{h^3 w}{12\eta}$$
Eq.8

Where Δp, h, w, l and η correspond to pressure drop, height of cross section, width of cross section, length of the nanochannel and viscosity, respectively.
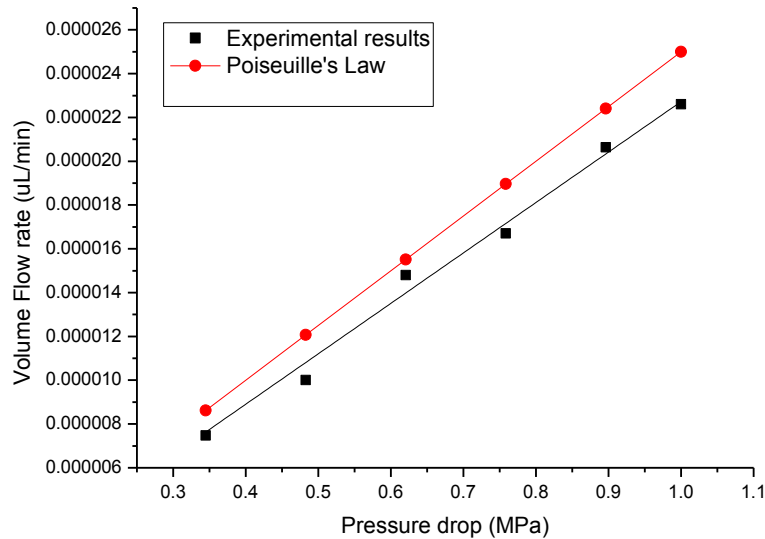

Figure 3. Average volume flow rate vs. pressure drop in a nanochannel.

The red dots and curve in Figure 3 shows the theoretical line based on integrated Hagen–Poiseuille's equation, where 1.0×10^{-3} Ns/m^2 viscosity was used since the experiments were conducted at a 20 ^{o}C. The black dots and curve shows the experimental

results. The experimental average volume flow rate was slightly lower than theoretical results. This phenomena is also reported in other publications, [29,34,36] which they suggested the property of solution – apparent viscosity may change depending on the size of the channels. Another possible reason may be due to the partially collapse of the channel cross sections. Since the aspect ratio of nanochannel is relatively big (w/h = 50), little buckling of pyrex glass may happen while the pyrex and silicon wafers were anodically bonded. [54] Thus, the effective area of nanochannel cross section may be smaller than calculated number, which will lead to the slower flow rate.

3.2 Two phase flow regime map in the nano-scale channels

In this section, experiments of nitrogen/water two phase flows in nanochannels are conducted and flow profile images are illustrating in Figure 4.Three types of flow profiles were observed in the nano-scale channels under experimental conditions and some of them are also being found in millimeter and micro-meter sized channels in previously publications. [62, 63]

Annular flow was observed when the gas superficial velocity was relatively high (>0.116m/s) within the whole liquid superficial velocity range. A continuous gas core occupied most of the channel while a liquid "film" with a thickness ranging from 0.9 to 1.6 μm formed at the sidewalls. Note that the thinnest dimension of the "film" was still in the direction perpendicular to the observer (100 nm) thus the "film" was in fact zones near the sides of the channel that are not swept by the gas. It is noticed that the thickness of liquid films decreased with increasing gas superficial velocity. The hydrophilic inner wall determined the formation of liquid films and when the gas velocity was high enough,

gas will penetrated the liquid phase to form a gas core and the flow pattern will change from segmented flow to annular flow.
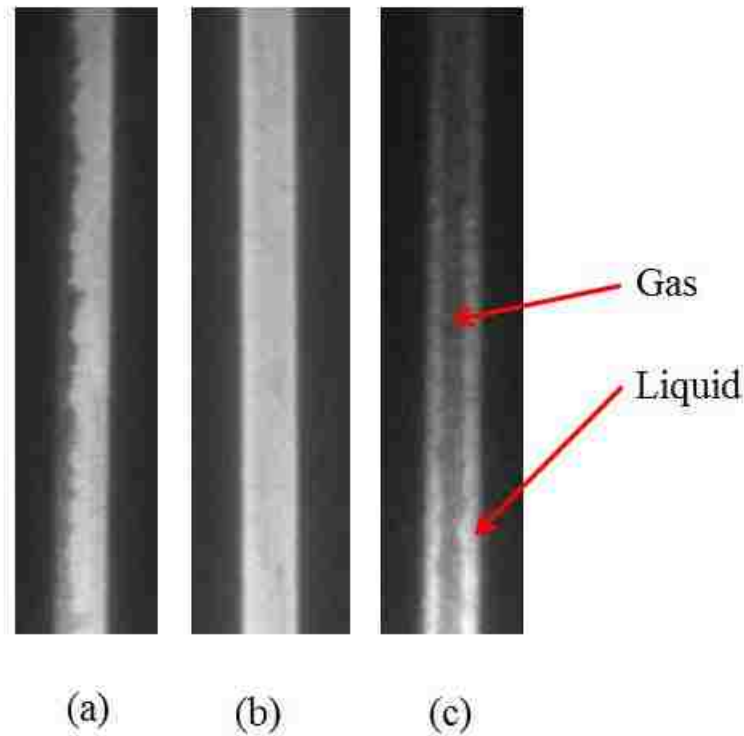
Figure 4. Water/gas two phase flow patterns. (a) Stratified flow; (b) Single phase flow; (c) Annular flow.

The stratified (wavy) flow pattern was found when both gas and liquid phases had small velocities (JG<0.0068m/s and JL<0.00027m/s). The interface between gas and liquid was not flat/smooth. At low gas velocity (JG<0.0094m/s) and a relatively high liquid velocity (JL>0.00031m/s), an interesting pattern was observed - single phase flow pattern. Liquid occupied the entire cross-section while gas phase was not found in nano-scale channels. Overall slug flow and dispersed bubbly flow were not observed - which

are two typical flow patterns in mm and μm size. Those two patterns are commonly appeared in the case with a relatively high liquid velocity and low gas superficial velocity. For slug flow, the gas slugs occupy the most of the channel cross-section and are separated by the liquid plugs. When the liquid velocity increase, gas slugs and bubbles are deformed and scattered in the continuous liquid phase. The reasons that slug flow and bubbly flow were not observed in the nano-channels were due to geometry features – the small dimensions and the relatively high aspect ratio of the channel cross section (w/h = 50). When reach to small dimensions, the rigidity of gas bubble is relatively high and gas bubbles will try to keep the spherical shape to reduce surface tension. The nano-channels in our experiment are too wide for gas bubble to occupy the entire cross-section. Also, at low velocities, since the inner wall of the nano-channels appeared to be hydrophilic, the liquid phase (water) can be spontaneously imbibed into the nano-channels whereas any gas motion must overcome the capillary forces. This explained why single liquid phase was found in some cases –the nano-channels were filled by liquid phase as the driving pressure was too low for the gas phase to enter the nanochannels.

Based on flow profile and superficial velocities, flow regime map is identified from a total of 49 experiments and is showing in Figure 5. The observed flow regimes corresponded to these ranges of superficial gas and liquid velocities are: gas superficial velocity (JG) 0.005 ~ 0.02m/s and liquid superficial velocity (JL) 1.0E-5 ~ 9.4E-4 m/s, respectively.

It is noticed that both gas and liquid velocities were ultra-small in the experiments compare to the flow regime results in conventional-sized channels which had sub-mm

and mm inner diameter. Typically only one flow pattern is presented at such low velocities in conventional-sized channels – and mostly is segmented flow (bubbly or slug). Serizawa et al.[51] reported bubbly flow pattern observed while the J_G ranging from 0.001 to 0.5 m/s and J_L ranging from 1.0E-4 to 0.1 m/s. Stratified flow was predicted from Mandhane et al.[52] under similar conditions. However, in ultra-small channels (5μm × 100nm), the flow regimes are much more sensitive to the slight velocities difference between water and gas, which three different flow patterns were found. By comparing the flow regime map between presented results and conventional-sized pipes, the presence of annular flow and stratified flow had partial agreement with the flow regime in larger channels,[64-66] although stratified flow and wavy flow are not the case in the present study with negligible effect of gravity. Like we mentioned above, the aspect ratio and dimension of the channels significantly affect the formation of gas bubble and gas slug.[44, 51]
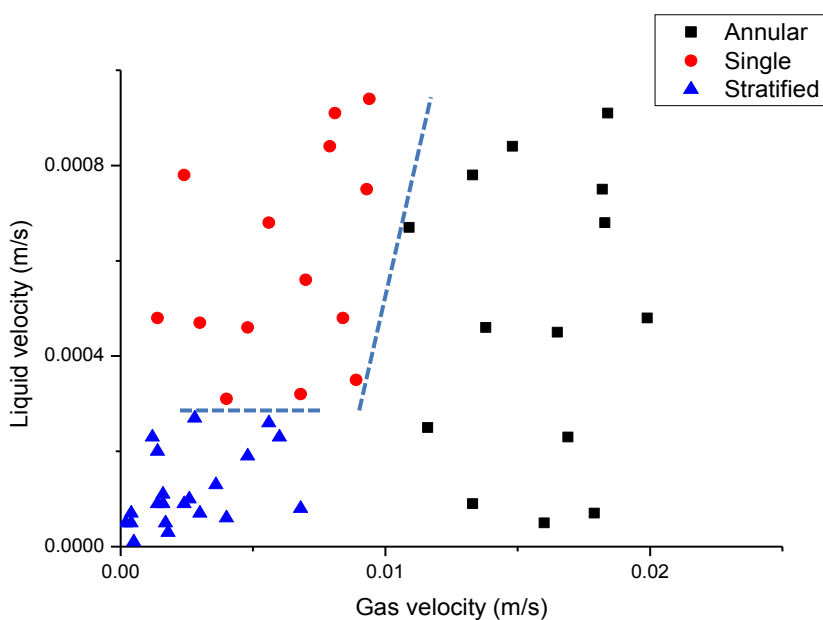
Figure 5. Water/gas two phase flow regime map in nano-scale channels.

4. CONCLUSION

A novel optical method for single and two phase flow in nanochannels are developed. Pressure drops in the nanochannels were controlled and stable pressure driven flows were achieved. Meanwhile, a concentration dependent fluorescence signal correlation method was developed to measure the volume flow rate in nanochannels. Single liquid phase and gas/liquid two phase pressure driven flows were performed in nanochannels. For the single liquid phase flow, linear correlations between flow rate and pressure drop was obtained which closely fit into to theoretical values from Poiseuille's Law. Gas/water two-phase flow were performed in nanochannels and flow patterns were characterized into three different types - single phase flow, wavy-stratified flow and

annular flow under ultra-low velocities, their detailed features are described. Two-phase flow regime map was also constructed. It was found that the two-phase flow structures in nanofractures are essentially different in many points from those of two-phase flows encountered in ordinary scale tubes and channels with mild cross-section aspect ratios. No segmented flow - bubbly flow or gas slug flow was observed in nanochannels under the conditions that they would normally occur. The result will provide crucial information for the analysis of multi-phase flow in nano-scale channels.

2. Optic Imaging of Two-phase Flow Behavior in One Dimensional Nano-scale Channels

ABSTRACT

Gas in tight sand and shale exists in underground reservoirs with microdarcy (μD) or even nanodarcy (nD) permeability ranges; these reservoirs are characterized by small pore throats and crack-like inter-connections between pores. The size of the pore throats in shale may differ from the size of the saturating fluid molecules by only slightly more than one order of magnitude. The physics of fluid flow in these rocks, with measured permeability in the nanodarcy range, is poorly understood. Knowing the fluid flow behavior in the nano-range channels is of major importance for stimulation design, gas production optimization and calculations of the relative permeability of gas in tight shale gas systems. In this work, a lab-on-chip approach for direct visualization of the fluid flow behavior in nanochannels was developed using an advanced epi-fluorescence microscopy method combined with a nano-fluidic chip. Displacements of two-phase flow in 100 nm depth slit-like channels were reported. Specifically, the two-phase gas slip effect was investigated. Under experimental conditions, the gas slippage factor increased as the water saturation increased. The two-phase flow mechanism in one dimensional nano-scale slit-like channels was proposed and proved by the flow pattern images. The results are crucial for permeability measurement and understanding fluid flow behavior for unconventional shale gas systems with nano-scale pores.

1. INTRODUCTION

Compared with conventional gas reservoirs, shale gas reservoirs contain a lot of ultra-small pores with sizes in the range of 1 to 300 nanometers. Additionally, the matrix permeabilities of those unconventional gas reservoirs are in the microdarcy (μD) to nanodarcy (nD) range. When fluids (gas, water) flow in a shale pore, the flow diameter is only about one or two order of magnitude larger than the molecule size (0.4~3nm).Under those conditions, effects of free mean path of gas molecules on the gas flow is not negligible and Darcy's equation may not be accurate or practical for describing the fluid flow behavior [67]. Other flow mechanisms have been reported such as slip flow and diffusive flow [68].

Extensive studies have been conducted on single-phase flow in tight sand and shale gas systems [31, 69-71], and equations have been derived to measure the relative permeability of gas and to determine the single-phase gas slippage effect [72]. Swami and Clarkson [73] summarized and compared several methods for quantifying non-Darcy flow in unconventional gas reservoirs. Jones and Owens [70] conducted permeability measurements on over 100 samples from various tight shale plays and derived empirical relationships between the slippage factor and reference permeability. Javadpour [68, 74] introduced a new term, *apparent permeability*, to describe the complexity of gas flow in nanochannels, by incorporating both Knudsen diffusion and slippage. From the molecular dynamic simulation results, the ratio of apparent permeability to Darcy permeability increases sharply as pore sizes decrease to smaller than 100nm.

Under real shale gas reservoir conditions, two phases (mostly water and gas) typically exist. It has been reported that in some ultra-low permeability shale gas

reservoirs, water saturation could be much greater than that in conventional shale gas plays. The effects of water saturation on the gas permeability/relative permeability and gas slippage still have not been investigated sufficiently. Several studies have reported that the gas slippage factor for two-phase flow is affected by relative permeability and water saturation [67, 75-79]. Some of these researchers found that the two-phase gas slippage factor tends to decrease as water saturation increases. However, Li and Horne [76] reported contradictory results that the two-phase gas slippage factor increased as water saturation increased. Thus, more research in this area is required.

For laboratory experiments, shale samples were used in most cases in order to represent the real pore structure and distribution in the reservoir. However, there are some limitations of using shale samples in laboratory experiments. For example, water saturation and saturation distribution are difficult to measure. Meanwhile, the lab-on-chip technique is becoming a suitable approach for investigating fluid flow in ultra-small pores. Nanofluidic and microfluidic devices have been used in different areas for both fundamental research and application. Micro-models have been used to simulate numerous porous media transport phenomena, including microorganism transport in unsaturated porous media [80], bacteria dispersion in bioremediation strategies [81], and enhanced oil recovery [82]. Furthermore, the lab-on-chip technique provides a means by which to directly visualize fluid flow behavior, such as the displacement of one fluid by another, because most micro/nanofluidic chips are made of transparent materials. Some micro-models are being used to study multiphase flow under both saturated and unsaturated conditions; also imaging method has been used for the study of pore microstructure and fluid distribution [83-86]. Buchgraber et al., [86] have reported the

displacement of viscous oil by associative polymer solutions in a two dimensional etched-silicon micro-model. The grain sizes of their micro-models range of 50 to 300 μm where the average channel depth is 25 μm. The oil recovery and sweep efficiency were measured from the imaging data.

However, visualization studies of fluid flow in nanochannels are still lacking. This is mainly limited by the resolution of the imaging techniques. Traditional optic imaging methods under white light field mainly depend on reflect index differences or the adsorptions of certain wavelength of incident light, which will not be sensitive enough to distinguish different phases under nano-scale sizes. On the other hand, fluorescent tracers - also recognized as epi-fluorescence microscopy method has been widely used in biological and biomedical studies. These fluorescent dyes are small molecules that can have a strong emission of light after absorbing certain wavelength of light (excitation light), and the wavelength of emitted light is different from the wavelength of the excitation light. By extracting the emission light signal from the excitation light, high signal to noise ratio can be archived. The epi-fluorescence microscopy methods have been proved to have ultra-high sensitivity of even single bio-molecule detection. Funatsu et al., [87] reported the visualization of single fluorescently labeled myosin (a protein molecule) by using the developed epi-fluorescence microscopy method. Therefore, the epi-fluorescence method was used for the purposes of this study.

In this paper, we will introduce a lab-on-chip approach for direct visualization of the fluid flow behavior in one dimensional nano-scale channels (as nano-slit), which was developed by using the advanced epi-fluorescence microscopy method combined with

nanofluidic chips. We will report the two-phase displacements in 100 nm-deep channels and the effects of remained water saturation on the two-phase gas slippage in the 100nm-deep channels.

2. EXPERIMENTAL METHODS

2.1 Materials

High-purity nitrogen gas was used as the gas phase. Ultra-pure water pre-filtered by a 0.22μm pore size Nylon filter was served as the liquid phase. Alexa Fluor 488 was purchased from Invitrogen (Grand Island, NY) to serve as fluorescent dye at the final concentration of 1mg/L in the liquid phase.

2.2 Experimental apparatus and test section

The experimental system of epi-fluoresence microscopy combined with the nanofluidic chip was similar to the previous setup in our published work [88]. Figure 1 shows the schematic of experimental apparatus. Nitrogen gas tank was used for the injection of gas phase and the injection pressure was adjusted by the gas pressure regulator. Water was injected from a syringe pump (KDS100, KD Scientific) with a controllable injection rate ranging from 0.01ul/h to 10ml/min. The injection pressures of both gas and water were measured by pressure sensors. As mentioned above, epi-fluorescence microscopy method was used for images collection. The wavelength of the excitation light is at 488nm and the wavelength of the emission light is at 525nm. FITC dichroic mirror was used to filter out the excitation light (incident light) to reduce the background noises. All images were captured by a reverse microscope (Olympus, IX-51)

and high-speed ICCD camera. The gain and exposure times were set at 80 and 50 ms, respectively. Data were acquired through the Cellsens software provided by Olympus.

The schematic of the entire nanofluidic chip was shown in Figure 2. The nanochannels array consisted of 100 nanochannels with a dimension of 100 nm (depth) $\times$ 5 µm (width)$\times 200$ µm (length) were built into the nanofluidic chip. Two microchannels with a dimension of 10 µm (depth) $\times$ 50 µm (width)$\times$45 mm (length) for fluid introduction were connected to the nanochannels. The microchannels had equal lengths in order to balance the pressure drop. The microchannels are perpendicularly connected to the nanochannels to avoid direct injection. Because the primary objective of this study was to investigate two-phase flows in nanochannels, the nanochannels array served as the test section -it was considered as a porous media consisting of 100 nanochannels. The test section was $1500\,\mu m$ wide and $10\,\mu m$ high, the length of the test section was equal to the length of each nanochannel, which was $200\,\mu m$. In the experiments, two microchannels were not considered as part of the test section and were used instead to introduce fluids and control the pressure drop.

The method used to control the pressure drop across the test section was demonstrated in Figure 2. If the end pressures of a single nanochannel i are named P_{i1} and P_{i2}, the distance from the inlet to this nanochannel is L_i, and the total length of each microchannel is L, the pressure drop Δp_i will be equal to $\dfrac{(p_1 - p_2)\,(L - L_i)}{L}$ The nanochannel array is very small (<1.5mm) compared to the length of the microchannel (30mm), and when the nanochannel array is connected to the center of the microchannel,

the pressure difference across the nanochannels is nearly identical. Because $L_i \approx \frac{1}{2}L$,

the pressure drop across the nanochannel array is simplified as: $\Delta p = \frac{p_1 - p_2}{2}$. The

flow rate of the gas phase was determined by measuring the size and movement of the

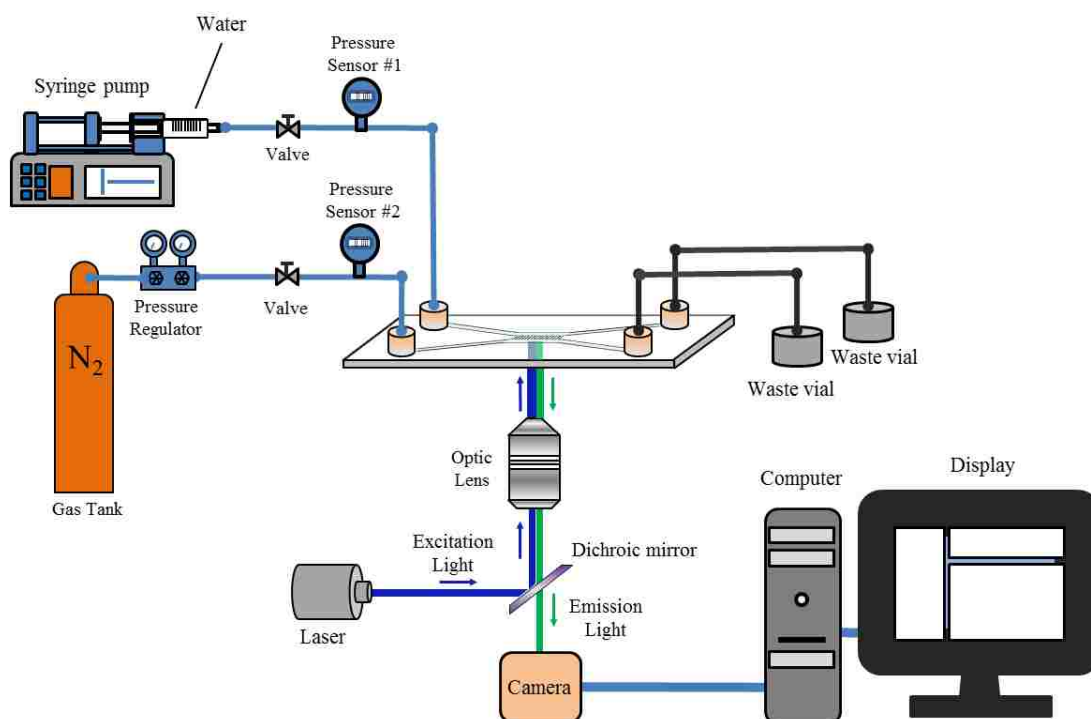gas slug in microchannel 2, which served as a batch collector.

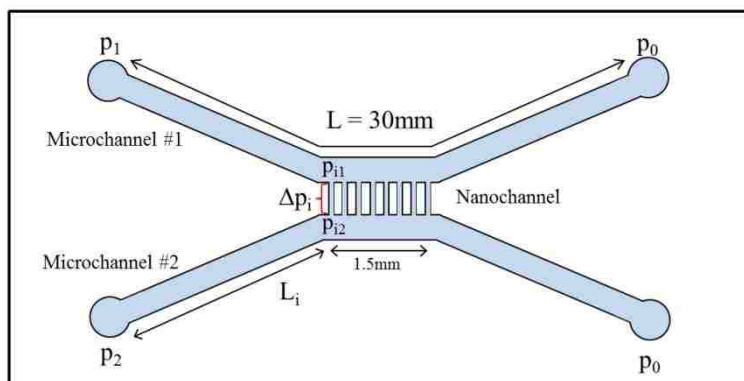Figure 1: Schematic of the experimental apparatus.

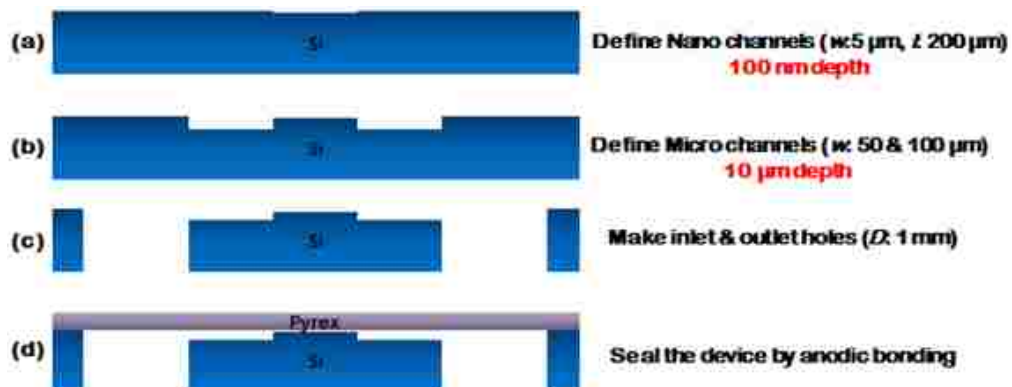Figure 2: Top view of nanofluidic chip and pressure control.

Figure 3: Cross-sectional schematic of Si-Pyrex micro- and nano-channel fabrication process.

2.3 Nanofluidic model fabrication

The nanofluidic chip consisting of micro- and nanochannels with the given dimensions were formed in double-sided polished <100> silicon wafers (thickness = 250 μm) with low-stress silicon nitride (~100 nm) on both sides. The fabrication process on the cross sectional view is demonstrated in Figure 3. First, an array of 100 nanochannels spaced 10 μm edge-to-edge was defined by a deep reactive ion etching through the back side of the wafer. Second, two microchannels were defined at either end of the nanochannel array. Third, the inlet and outlet holes were defined at both ends of the microchannels. Each device was removed from the wafer by cleavage along crystal planes. Finally the front side of each device (40 mm × 20 mm × 0.25 mm) was anodically bonded (330 ℃, 1 kV, 1 hour) to a thin Pyrex cover slip (Pyrex 7740, 40 mm × 20 mm × 0.3 mm, Newport Industrial Glass, Inc, Stanton, CA). In order to maintain the surface conditions of the nano-scale channels, the whole nanochip was rinsed by lab reagent water, methanol and nitrogen gas prior to use.

2.4 Nanochannels characterization

After the nanochannels were fabricated, the properties of the nanochannels were characterized by various techniques. The size and surface roughness of nanochannels have been examined by using the SEM before the nanochip was bonded. Figure 4 (a) ~ (d) presented the SEM images of the fabricated nanochannels. From the SEM images, the dimension of each fabricated nanochannel is 100 nm (depth) × 5 μm (width)× 200 μm (length) with less than 5% deviation. The roughness of the nanochannel surface is found to less than 1nm, which is measured by AFM. As it is showed in Figure 4(e), the wettability of the nanochannel surface has been characterized by measuring the static

contact angle. The measured static water contact angle (46°) indicates that the nanochannel is water wet. Also the contact angle measurements within different nanochannels have a deviation less than 5%, which indicates the wettability of the nanochannels is uniform.
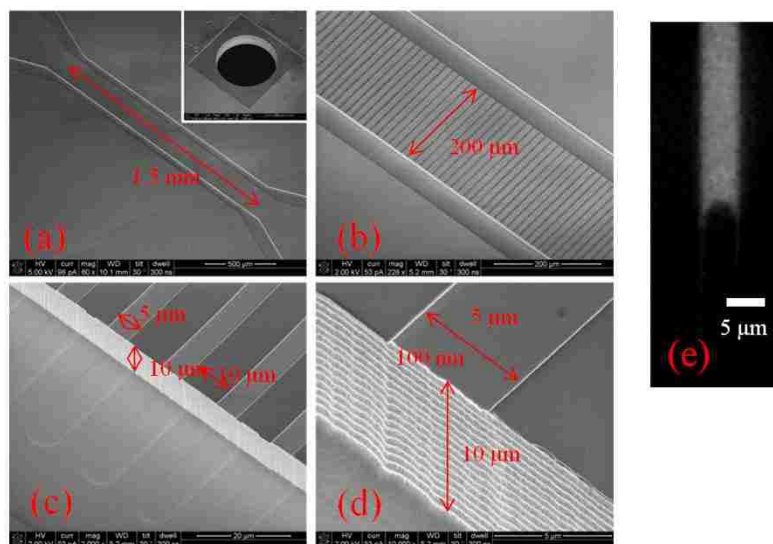
Figure 4: Nanochannels characterizations. (a)~(d): SEM images of fabricated micro- and nano-channels; (e) Static water contact angle measurement in the nanochannel.

2.5 Experimental procedure

Before every set of experiments, preliminary tests were conducted with the nanofluidic chip; no leakage was observed, and the flow was stable. The nanochip was cleaned by 0.1mole/L HCl, methanol and de-ionized water prior to use. All experiments were conducted at room temperature.

For gas displacing water, the nanochannels first were 100% saturated with water by forced imbibition into the pre-vacuumed nanofluidic chip; then nitrogen gas was pressure-injected into them to simulate the flow back. In order to calculate the intrinsic gas permeability at different water saturation levels, the apparent gas permeability was measured under different mean pressure p_{mi} at the same remaining water saturations S_{wi}. Various remaining water saturations were obtained by applying different pressure drops (Δp_i) on the test section. The applied mean pressure was always smaller than the pressure drop used to obtain the given remaining water saturation ($p_{mi} < \Delta p_i$) and images were taken by the microscope to ensure that the water/gas ratio did not change after the experiments.

For the water displacing gas experiments, the nanochannels were saturated with nitrogen gas. The gas phase was displaced by water at a constant pressure drop until a constant gas/water ratio was obtained. Gas saturation was determined from the image data.

2.6 Data processing– saturation determination

The phase saturation in the nanochannels was determined by processing images using ImageJ software. The procedure was demonstrated in Figure 5.

First, all captured images were converted into binary black/white images by thresholding the signal intensities across the image (Figure (a) to (b)). Water with fluorescent dye will be bright region while gas phase without fluorescent dye will be the dark region in the nanochannels.

Second, the total area of the nanochannels on the X-Y plane (A_t) was calculated by analyzing the area of water phase when the water saturation is considered as 100% (no gas phase was observed in the nanochannels), as it is shown in Figure 5 (b).

Third, the area of water phase in the nanochannels (A_i) was analyzed for each image - Figure 5(d). Since the height of the nanochannels is very small (100nm) compared with the width (5 μm) and length (200 μm), the variation of water saturation on the Z axis can be negligible. Thus, the water saturation (S_w) was determined by the ratio of area of water phase to the area of the nanochannels on X-Y axis:

$$S_w = \frac{A_i}{A_t} \times 100\%$$
Eq.1

After water saturation is determined, gas phase saturation (S_g) is calculated by 1-S_w.
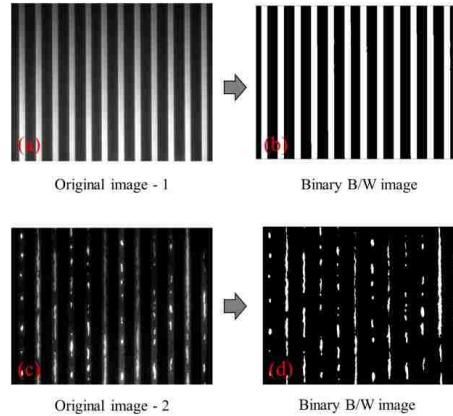
Figure 5: Image processing. (a) Original image of 100% water saturation in nanochannels; (b) Binary Black/White image of (a); (c) Original image of remained water saturation in nanochannels; (d) Binary Black/White image of (c).

3. RESULTS AND DISCUSSION

3.1 Theory

The gas slippage effect was first studied by Klinkenberg [3], and the Klinkenberg equation is expressed as follows:

$$k_g = k_{g\infty} \cdot (1 + \frac{4c\lambda}{r})$$

Eq. 2

Where k_g is the apparent gas permeability at a mean pressure, p_m; $p_m = \frac{(p_i + p_o)}{2}$; p_i and p_o are inlet and outlet pressures of the test section, respectively. $k_{g\infty}$ is the intrinsic permeability of gas at infinite pressure, λ is the mean free path of the gas molecule; r is the radius of the pore; and c is a constant.

Klinkenberg reduced Eq. 2 to:

$$k_g = k_{g\infty} \cdot (1 + \frac{b}{p_m})$$

Eq.3

Where b is the gas slippage factor, which is defined as:

$$b = \frac{4c\lambda p_m}{r} = \frac{4c'}{r}$$

Eq.4

The mean free path of the gas is inversely proportional to the mean pressure, p_m, so the factor c' represents a constant at a certain mean pressure. Based on Eq. 4, the gas slippage factor is inversely proportional to the radius of the pore. Li and Horne claimed that the slippage factor must decrease as the effective pore radius decreases.

According to Darcy's equation, in the gas/water two-phase flow, the effective gas phase permeability is calculated as:

$$k_g(S_w, p_m) = \frac{2q_2 \cdot \mu_g \cdot L \cdot p_2}{A(p_1^2 - p_2^2)} = \frac{q_2 \cdot \mu_g \cdot L \cdot p_2}{A(p_1 - p_2)(\frac{p_1 + p_2}{2})} = \frac{q_2 \cdot \mu_g \cdot L \cdot p_2}{A \cdot \Delta p \cdot p_m} \qquad \text{Eq.5}$$

Where k_g is the effective gas phase permeability at a water saturation of S_w and a mean pressure of p_m; q_2 and μ_g are the flow rate at the outlet and viscosity of the gas phase, respectively; p_1, p_2, p_m and Δp are the inlet pressure, outlet pressure, mean pressure and pressure drop, respectively; L and A are the cross-sectional area and length of the flow, respectively. Considering the gas slippage effect, the intrinsic effective permeability of the gas phase, which is pressure-independent, is presented with the following equation:

$$k_{g\infty}(S_w) = \frac{k_g(S_w, p_m)}{(1 + \frac{b_{Sw}}{p_m})} \qquad \text{Eq.6}$$

Where $k_{g\infty}(S_w)$ represents the intrinsic permeability of the gas phase, and b_{Sw} is the gas slippage factor for a water saturation of S_w. The gas slippage effect should not be neglected in low-permeability unconventional shale gas reservoirs, so the relative permeability of gas can be computed using Eq. 6.

Based on the experimental conditions and geometry of the test section used in our work, the Knudsen number has been calculated. The Knudsen number is an important factor that categories the flow regime:

$$K_n = \frac{\lambda}{d} \qquad\qquad \text{Eq.7}$$

Where d is the pore diameter, and λ is the mean free path of the gas molecules, which is defined as:

$$\lambda = \frac{\mu}{p_m} \sqrt{\frac{\pi RT}{2M}} \qquad\qquad \text{Eq.8}$$

Where μ is the viscosity of gas, p_m is the mean pressure, R is the universal gas constant (R=8.314J/mol/K), T is the absolute temperature, and M is the molecular mass of the gas. The correlation between the Knudsen number and the flow regime was summarized in Table 1 [86]. The Knudsen number in this work is calculated ranging from 0.05 to 0.11. Based on the Knudsen number, most of the flow regime falls into the slippage flow region. In this flow regime, the viscous flow theory must be modified to accommodate the slippage boundary conditions. Many tight gas plays fall into this region, and Klinkenberg's slippage theory holds well for most of them. Eq. 5 is used to calculate the apparent gas permeability and the intrinsic gas permeability.

This study also investigated the flow mechanism because the optic lab-on-chip method allows direct visualization of the two-phase flow behavior in the nanochannels. Dullien et al., [89] posited that there are two major flow structures for the flow of two immiscible fluids in porous media: channel flow and funicular flow. In channel flow, each phase moves through its own separate network of interconnecting channels. As the water saturation increases, so does the number of channels filling with water, but the number of channels filling with gas decreases. Under these conditions, saturation water

tends to fill the smaller channels because it is the wetting phase, and the gas phase tends to occupy the larger pores. Thus, the average radius of the gas channel increases as the water saturation increases. Based on Eq. 4, the slippage factor is inversely proportional to the average radius of the channel. Therefore, the slippage factor may decrease with an increase in water saturation.

Table 1: Flow regime based on Knudsen number

Knudsen number (K_n) range	Flow regime
≤ 0.001	Viscous flow
$0.001 < K_n < 0.1$	Slip flow
$0.1 < K_n < 10$	Transition flow
$K_n \geq 10$	Knudsen's (free molecular) flow

In funicular flow, the channel/pore is occupied by flows of both gas and water; the water is near the inner wall, and the gas is on the inside and occupies the central portion of each channel. Under these conditions, and also noted by Li and Horne [76], the thickness of the water layer increases as the amount of saturated water increases, which causes the effective radius of the gas channel to decrease. Thus, the gas slippage factor increases.

In real shale/core samples, obtaining an accurate water saturation and distribution of water saturation is very difficult. As a result, it is almost impossible to determine which type of flow (channel or funicular) is governing in the immiscible two-phase flow in shale/core samples. In our work, the flow pattern was observed from the real-time imaging data, which will be discussed in the next section.

3.2 Water displacing gas

Water displacing gas experiments were conducted in the 100nm deep nanochannels. The nanochannels were 100% saturated with nitrogen gas, and no water was observed in the test section. De-ionized water with fluorescent dye (1mg/L Alexa fluor 488) was injected into the nanochannels under pressure. The pressure drop ranged from 0.8 psi to 57.5 psi. The flow rate, flow patterns and gas saturations were obtained from the imaging data. Figure 6 shows the displacement patterns of water phase displacing gas in the nanochannels before the breakthrough (unstable stage). As it is shown in Figure 6(a), a frontal displacement (piston-like) was observed in most cases, which was reasonable because each nanochannel consisted of one independent straight channel and uniform cross sections, so the sweep efficiency was supposed to be high (around 100%).When the pressure drop was relatively low, a specific displacement pattern- a liquid core with a cavity on the side was observed in Figure 6(b), where water did not occupy the entire nanochannel; instead, a liquid core was formed while the gas phase encompassed the edge of the channel. Based on our knowledge, this type of patterns has not been observed in the conventional sized channels. This was probably due to the geometry of the nanochannels. In the 100nm-deep channel, the effect of the surface energy on the fluid flow was not negligible. The aspect ratio of the channel was relatively

large (width/depth = 50), so a liquid-core pattern decreased the surface of the interfaces, thus decreasing the surface energy. It is noticed that with this type of flow pattern, gas phase may be trapped near the edge of the nanochannels, which will yield higher gas saturation than the first type of flow patterns. This also explained that why most of residual gas phases were either small gas bubbles or gas slugs that attached to the side wall of the nanochannels.

Figure 7 shows the gas saturation during the process of water displacing gas. Figure 7(a) is the image of remained gas saturation after spontaneous imbibition, where Figure 7(b) shows the image of irreducible gas saturation in nanochannels. Figure 7(c) summarizes the remaining gas saturation under various water injection pressures. Overall, the residual saturation of gas in nanochannels was very low (10 %<) under all experimental conditions, which were mainly due to the fact that the surface of nanochannel is water-wet. And the geometric features of the nanochannels also played an important role - the aspect ratio of the cross section was relatively high (width / height = 50). When reaching smaller dimensions, the rigidity of the gas bubble was relatively high as gas bubbles will try to keep their spherical shape to reduce surface tension. The nano-channels in our experiment were too wide for gas bubbles to occupy the entire cross section. The imaging data revealed that the residual gas existing in the nanochannels after the water displacing gas procedure took one of two forms: (a) small bubbles or (b) gas layers.
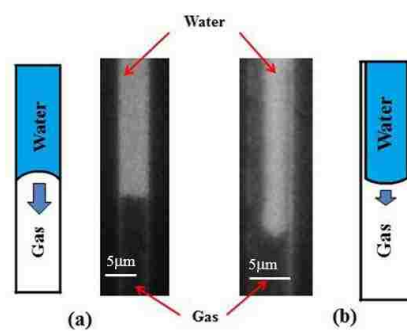
Figure 6. Water displacing gas patterns, two different interface patterns. (a) Frontal displacement interface under pressure drop of 12.5psi; (b) Liquid plug with cavity under pressure drop of 0.8 psi.
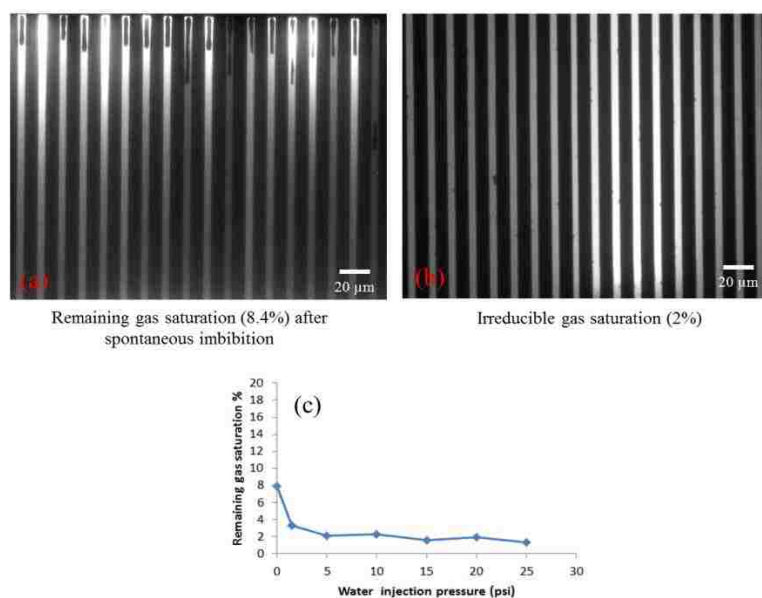

Figure 7. Gas saturation during water displacing gas. (a) Remained gas saturation in nanochannels after spontaneous imbibition; (b) Irreducible gas saturation in nanochannels; (c) Remaining gas saturation under various water injection pressures.

3.3 Gas displacing water

Experiments of gas displacing water (flow back process) were also conducted in 100nm deep nanochannels. Nitrogen gas was injected under various pressure drops ranging from 10 psi to 90 psi. The flow rate and flow profiles of gas displacing water were obtained from microscopic images. The two-phase flow patterns of gas displacing water in nanochannels are demonstrated in Figure 8. Three types of flow patterns were observed. In the first case, (a), gas flow occupied one side of the channel after breakthrough, while the water phase was trapped on the other side of the channel. In the second case, (b), a gas core filled the middle of the nanochannels, surrounded by a water layer on the side walls. In the last case, the gas phase occupied the majority of the channel, and only a few discrete water plugs (c) were attached inside. All three flow patterns that observed in this work were also reported in the multi-phase flow in conventional sized tubes [90, 91].

The remaining water saturation at different pressure drop is presented in Figure 9. The drainage process starts from 100% water saturation – Figure 9 (a) and the irreducible water saturation is around 15% - Figure 9 (e). Overall the remaining water saturation in nanochannels is significantly higher than remaining gas saturation after water displacing gas. Under most experimental conditions, even though the sweep efficiency almost reached to 100%, the remained water saturations were over 40% - Figure 9 (b). It is noticed that the remained water saturation in the nanochannels is much higher than those obtained in the conventional sized tubes [77]. This can be explained by the effect of both wettability and nanochannels geometries. From Figure 4 (e), the nanochannels used in this work are water wet. Under nano-scale, the specific surface area (the ratio between

surface area to the pore volume) is much larger compared to the conventional sized channels and the effect of surface wettability will have larger impact on the saturation.
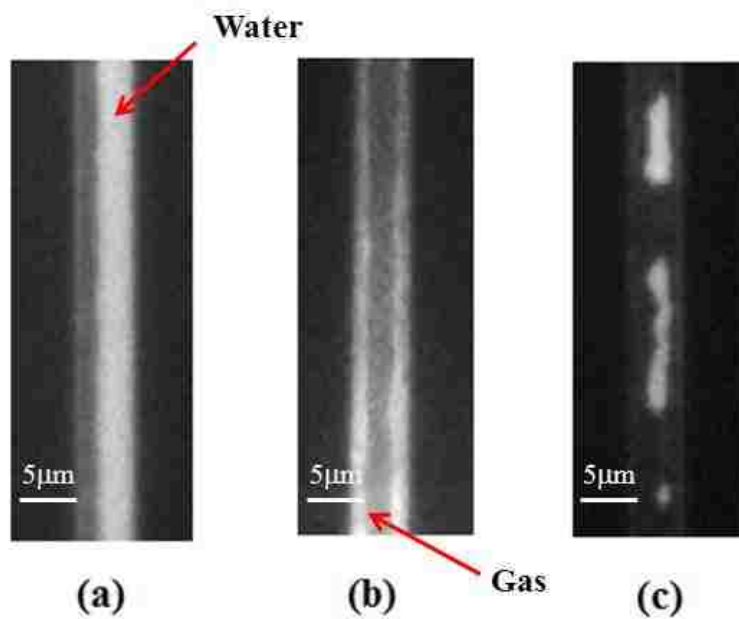
Figure 8. Flow patterns of immiscible two-phase flow in nanochannesl. (a) Side flow of gas; (b) Annular flow; (c) Water slug.
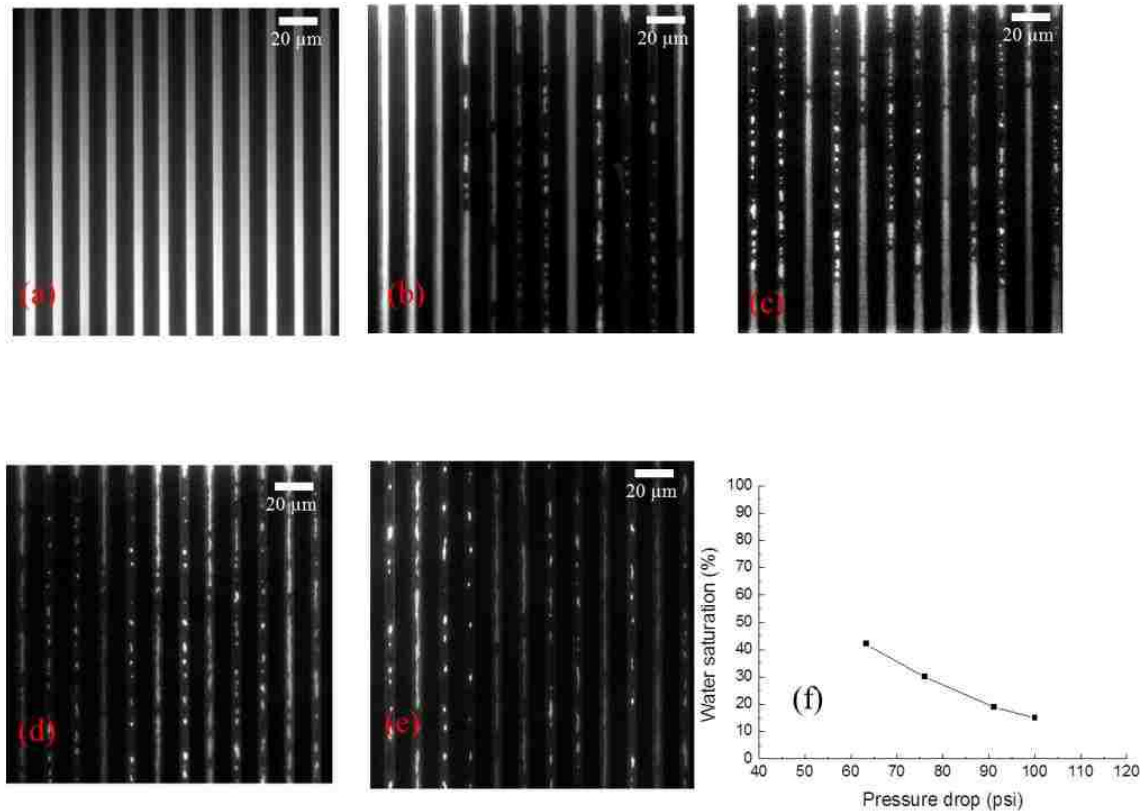
Figure 9.Water saturation during gas displacing water. (a) Image of 100% water saturation; (b) Image of 42% water saturation; (c) Image of 30% water saturation; (d) Image of 19% water saturation; (e) Image of 15% irreducible water saturation; (f) Water saturation under various pressure drop.

3.4 Two-phase gas slippage effect in nanochannels

In order to investigate the two-phase gas slippage effect, various water saturations were obtained using the method described below. Figures 10 through Figure 12 show the image data and also summarize the procedure by which to achieve water saturation. The lighter fields represent the water phase with the addition of fluorescent dye, and the darker fields in the channel represent the gas phase. In Step 1 of Figure 10, the test section was first pressure-filled by water from a microchannel (2); the water

saturation was approximately 94%. In Step 2 (Figure 11), the gas phase then was injected into the test section via a microchannel (1) under a stable pressure of p_1, which will be denoted as the starting pressure. Water saturation was reduced to a constant ratio, e.g., 29.7% in Figure 12; the gas permeability measurements at this water saturation level were conducted by applying several smaller pressures p_i ($p_i < p_1$). Because p_i is smaller than p_1, water saturation remained constant during the measurement (Figure 12). After a series of gas permeability measurements at the same water saturation level, another set of experiments was repeated from Step 1.

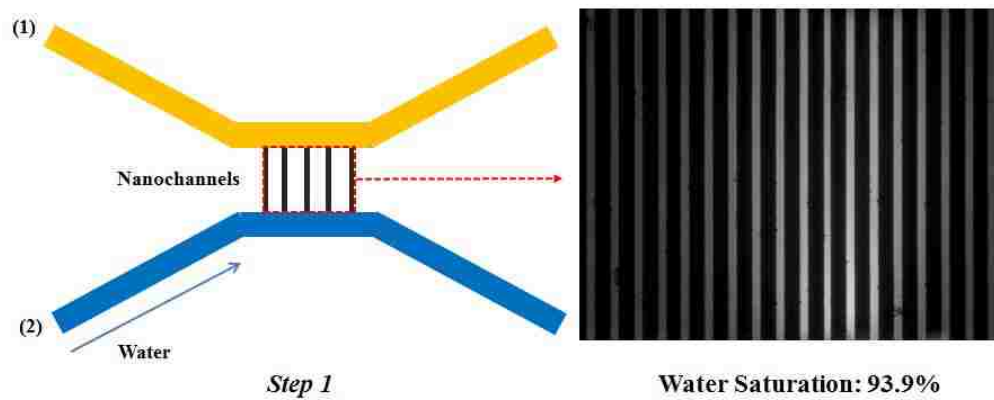Figure 10. Step 1 - Measurement of gas permeability at different water saturations.
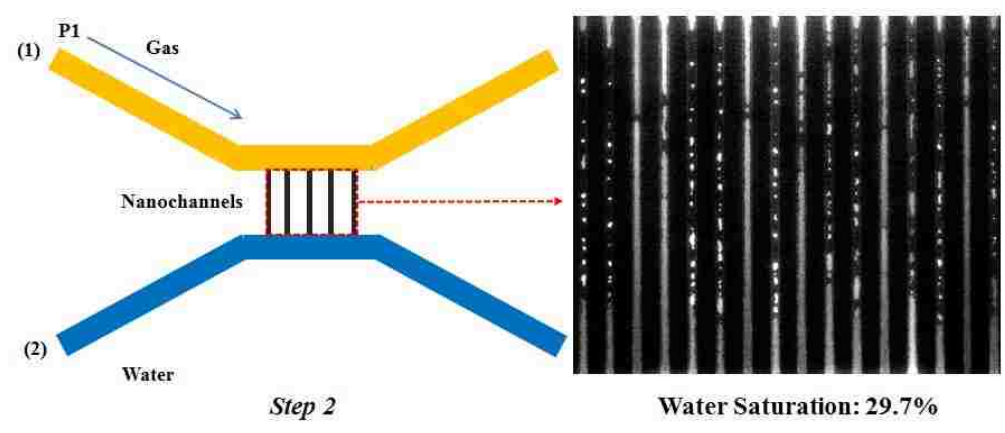
Figure 11. Step 2 - Measurement of gas permeability at different water saturations.
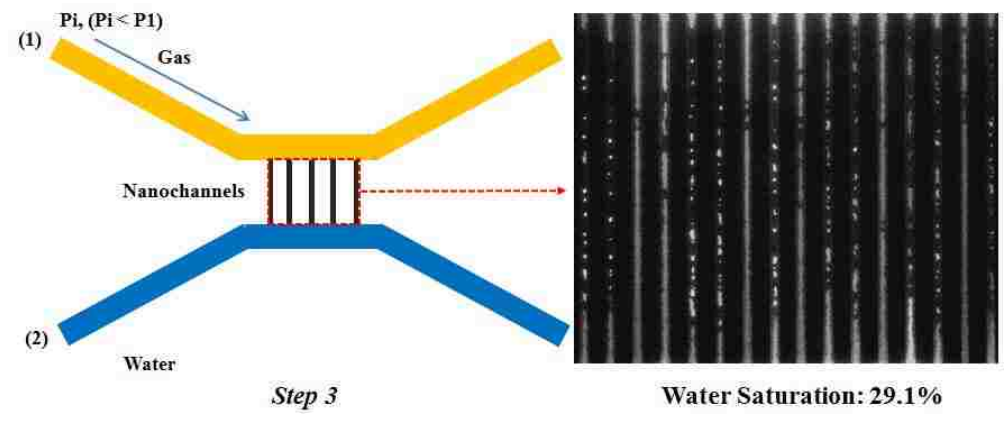
Figure 12. Step 3 - Measurement of gas permeability at different water saturations.

In order to obtain the intrinsic relative gas permeability, the (apparent) gas permeability was determined first without consideration of the gas slippage effect. Figure

13 summarizes the correlation between the apparent gas permeability and the reciprocal mean pressure at different water saturations ranging from 0 to 42%. The apparent gas permeability correlated linearly with the reciprocal mean pressure under all experimental conditions. There were fewer data points when the water saturation was high (42%) because the saturated water stayed immobile only in the range of low mean pressure.
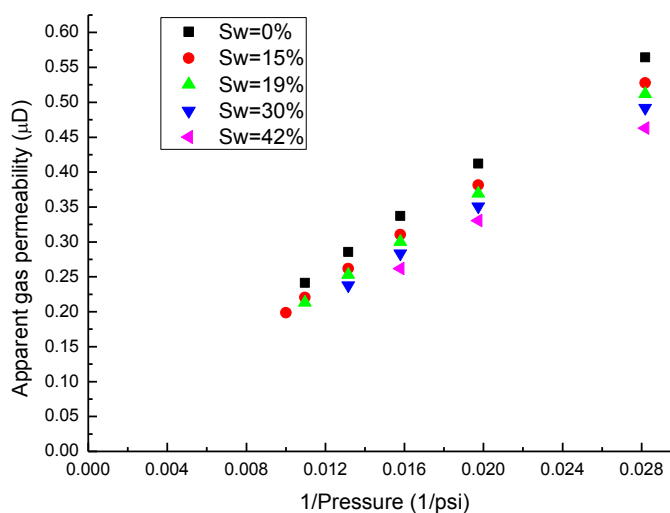
Figure 13. Gas slippage effect at different water saturations.

The intrinsic gas permeability at different water saturations was obtained by linear regression at infinite pressure ($1/P = 0$) on each curve of experimental data. It was found that the intrinsic gas permeability was affected by the water saturation.

Using the data shown in Figure 13, the gas slippage factors at different water saturations were calculated and presented in Figure 14. The gas slippage factor increased

with increases in the water saturation, which supports Klinkenberg's theory [3] and results reported by Li and Horne [76].
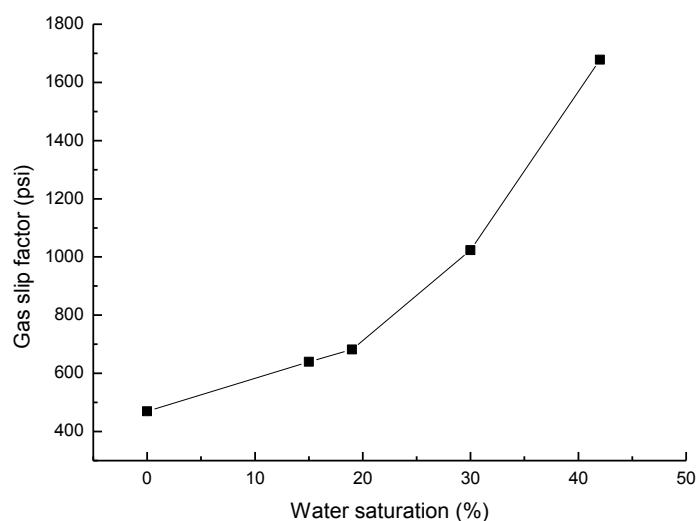
Figure 14. Correlation between water saturation and gas slippage factor.

As noted in the introduction, some researchers [67, 75, 78] have reported that the gas slippage factor decreases as water saturation increases. There are many possible reasons for this contradiction, such as the geometry and pore structure of the samples, method of establishing the liquid saturations, and distribution of the water saturation.

In this work we propose that the distribution of the water saturation is the primary factor that affects the correlation between gas slip factor and water saturation. Based on observations of all three types of flow patterns, the nanochannel was occupied by both the gas and water phases. This phenomenon indicates that the gas displacing water

experiments in this study fall into the funicular flow regime. Because the water phase occupied either one side or both sides of the channel in the form of a water layer, its existence clearly reduced the gas flow radius in the nanochannels. According to Klinkenberg's theory in Eq. 4, the slippage factor is inversely proportional to the effective radius of the flow, which then increases as the water saturation increases.

4. CONCLUSIONS

1. In order to better understanding the fluid flow behavior in the nano-scale channels, this work has demonstrated a novel approach to characterize fluid flow behavior in the one dimensional nano-scale channels by using epi-fluorescence microscopy combined with nanofluidic chip. 100nm-deep slit-like nanochannels were fabricated on the silica wafers and water/gas two phases flow in 100 nm-deep channels were successfully observed and characterized.

2. For the water/gas two phase displacements in nano-scale channels, different flow patterns and residual water/gas saturations were obtained from imaging data. Three types of flow patterns were observed for the gas displacing water while two types of flow patterns were found for the water displacing gas. Most flow patterns that observed in this work were also reported in the conventional sized tubes. However, a distinguish pattern was observed for liquid displacing gas - liquid core fills in the center with cavity on the side of the channels. We believe that this type of flow pattern is only found in the nano-scale channels and may cause higher gas residual saturations.

3. It was found that in the one dimensional nano-scale channels, there was over 40% of remaining water saturation after gas displacing water while only less than 10% of gas remaining saturation in water displacing gas experiments, which might partially explain why more than 50%hydraulic fluid cannot flow back. The remained water saturations are much higher compared with those in conventional sized tubes, which indicate that the surface wettability play a key role on the phase saturation when the size of the channel decrease to nano-scale.

4. The effect of remained water saturation on two-phase gas slippage in 100nm deep channels was also investigated. Under experimental conditions, the gas slippage factor increased with increases of remaining water saturation. This phenomenon can possibly be explained by that under the experimental conditions, the increase in water saturation dramatically reduced the effective radius of the gas channel. Based on Klinkenberg's theory, the gas slippage factor increases as the channel radius decreases, which was supported by the two-phase flow imaging data. It has to be noticed that more factors need to be considered and studied before a quantitative model can be developed.

This work provides a valuable view of fluid flow behavior in the nano-scale channels by using visualization methods. It also demonstrates the high potentials of using optic imaging method combined with micro/nanofluidic chips to solve the problems in unconventional reservoirs. Although more work need to be done to fill the gaps between laboratory experiments and theoretical models, the results of water/gas two-phase displacements and residual gas/water saturations in one dimensional nanochannels will be

helpful for achieving a better understanding of gas flow behavior in unconventional shale gas and tight gas plays.

NOMENCLATURE

p_1 = inlet pressure of micro-channel 1

p_2 = inlet pressure of micro-channel 2

p_0 = outlet pressure of micro-channel

p_{i1} = inlet pressure of nano-channel i

p_{i2} = outlet pressure of nano-channel i

p_m = mean pressure

Δp = pressure drop

K_g = apparent gas permeability

$k_{g\infty}$ = intrinsic gas permeability, absolute gas permeability

S_w = remaining water saturation

$k_{g\infty}(S_w)$ = intrinsic gas permeability at water saturation of Sw

$k_g(S_w,p_m)$ = apparent gas permeability at water saturation of Sw and mean pressure of pm

λ = mean free path of gas

r = radius of pore/channel

b = gas slip factor

b_{Sw} = gas slip factor (at water saturation of Sw)

q_g = flow rate of gas phase

μ_g = viscosity of gas phase

L = length of the channel

A = cross section area of the test section

K_n = Knudsen number

R = universal gas constant

T = the absolute temperature

M = molecular mass of gas

ϕ_g = effective gas porosity

ACKNOWLEDGEMENTS

Professor Ralph Jimenez and Jennifer Lubbeck in the Department of Chemistry & Biochemistry at the University of Colorado, Boulder for assistance with anodic bonding.

The corresponding authors for the paper are

Baojun Bai, Lester Birbeck Chair Professor, Program of Petroleum Engineering, Email: baib@mst.edu

Yinfa Ma, Curator Professor, Department of Chemistry, Email: Yinfa@mst.edu

3. **Visualization of Water/gas Two-phase Displacements in Nanopores**

ABSTRACT

Microfluidic devices have been increasingly used for the study of fluids flow in the area of biomedical, chemical, and engineering as artificial representations of natural porous media. On the other hand, the fluids flow in nanopores, such as in the unconventional gas or oil reservoirs, is poorly studied. In this paper, a novel optic imaging method has been applied to measure the water/gas two phase displacements in nanopores. The displacement of two-phase in nanopores has been directly visualized and recorded as a function of time. The displacement mechanisms were first discussed as some distinctive mechanisms were found in both imbibitions and drainage processes. The relationship between capillary pressure and phase saturation for the nanopores with various dimensions and pore structures is reported for the first time. It was found that the capillary pressure is not only dependent on the phase saturation, but also largely dependent on the pore structure and specific interfacial area. Meanwhile, an unsteady-state method has been demonstrated to measure the relative permeability of water/gas in nanopores. This is also the first time to present the measurement of relative permeability as a function of wetting phase saturation in nanopores. The results of this work are crucial for permeability measurement and understanding fluid flow behavior for unconventional shale gas systems with nanopores.

1 INTRODUCTION

Unconventional gas is an important energy resource that mostly mainly developed in North America. Compared with conventional gas reservoirs, unconventional gas reservoirs contain a lot of ultra-small pores with sizes in the range of 1 to 300 nanometers [1]. Additionally, the matrix permeabilities of those unconventional gas reservoirs are in the microdarcy (μD) to nanodarcy (nD) range. When fluids (gas, water) flow in a shale pore, the flow diameter is only about one or two order of magnitude larger than the molecule size (0.4~3nm). Under those conditions, effects of free mean path of gas molecules on the gas flow is not negligible and Darcy's equation may not be accurate or practical for describing the fluid flow behavior [67]. Other flow mechanisms have been reported such as slip flow and diffusive flow [68]. Thus the producing and extraction methods used for conventional gas reservoirs may not be suitable for the unconventional gas reservoirs. And understand of fluid flow, especially water/gas flow in nanopores are essential for design of hydraulic fracture stimulation and production.

Meanwhile, microfluidic devices have been widely used to study the fluids flow in fields of biomedical,[39, 40] chemical synthesis,[41] chemical engineering[42] and petroleum refinery.[43] Because most microfluidic devices are made of transparent materials, they provide a means by which to directly visualize fluid flow behavior, such as the displacement of one fluid by another. Some micro-models are being used to study multiphase flow under both saturated and unsaturated conditions; also imaging method has been used for the study of pore microstructure and fluid distribution [49, 55, 63, 65, 83-86, 92]. Buchgraber et al., [86] have reported the displacement of viscous oil by associative polymer solutions in a two dimensional etched-silicon micro-model. The

grain sizes of their micro-models range of 50 to 300 μm where the average channel depth is 25 μm. The oil recovery and sweep efficiency were measured from the imaging data. Dawe et al., [21] performed immiscible displacements of two phases in heterogeneous micro-models. The permeability was controlled by packing unconsolidated glass bead packs. The results demonstrated the effect of heterogeneities on the displacement patterns as well as the phase saturations. However, visualization studies of fluid flow in nanopores are still lacking.

In this paper, we will present an optic imaging method for direct visualization of the water/gas two-phase displacements in nanopores with various dimensions and pore structures. The displacement mechanisms in both imbibitions and drainage processes will be discussed based on image data. The relationship between capillary pressure and phase saturation for the nanopores with various dimensions and pore structures will also be reported. Meanwhile, an unsteady-state method will be demonstrated to measure the relative permeability of water/gas in nanopores for the first time.

2 EXPERIMENTAL METHODS

2.1 Chemicals and materials

High-purity nitrogen gas was used as the gas phase. Ultra-pure water pre-filtered by a 0.22μm pore size nylon filter was served as the liquid phase. Alexa Fluor 488 was purchased from Invitrogen (Grand Island, NY) and prepared the liquid phase as the fluorescent dye at the final concentration of 10mg/L.

2.2 Experimental apparatus

The experimental system includes the optic imaging system and pressure control/measurement system, which has been used for the visualization of fluids flow in nanopores in our published work [88]. Briefly, nitrogen gas tank with controllable injection pressure was used for the introduce of gas phase and syringe pump with controllable injection rate was used for the introduce of water. The injection pressures of both gas and water were measured by pressure sensors. The epi-fluorescence microscopy method was used for the visualization of fluids flow. The wavelength of the excitation light is at 488nm and the wavelength of the emission light is at 525nm. All images were captured by a reverse microscope (Olympus, IX-51) and high-speed ICCD camera. The camera exposure time was set in the range from 100to 200ms. Data were acquired through the Cellsens software provided by Olympus.

2.3 Nanofluidic chip design, fabrication and characterizations

The nanofluidic chips were designed and fabricated on to the silicon wafers by the deep reactive etching method that described in previous publication [88]. For each nanofluidic chip, two parallel microchannels were etched and perpendicularly connected to nanopores. The two microchannels are served for introduce of fluids and thus to reduce the chance of pore clogging caused by direct injection. Specifically, the nanopores on the fabricated nanofluidic chips have two types of structures: parallel straight channels and random network pattern and the depths were varied from 100nm, 300nm to 500nm.

After the nanopores were etched on the nanofluidic chips, the properties of the nanopores were characterized. The dimensions and the surface of nanopores have been

examined by SEM before the nanofluidic chip was bonded. Figure 1 (a) ~ (d) presented the SEM images of the fabricated random network nanopores with 300nm deep and 3 micron wide.

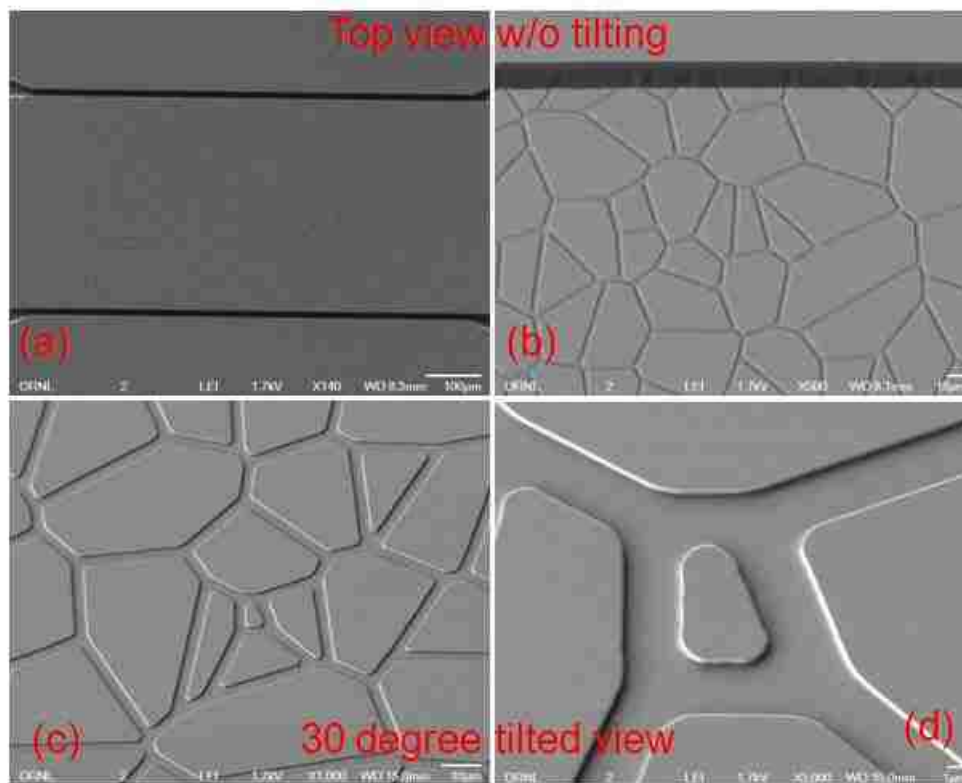Figure 1. SEM images of fabricated random network nanopores. (a) An overview of microchannels and nanopores from top; (b)~(d) enlarged SEM images of nanopores with 3μm width and 300nm depth.

2.4 Water/gas two phase drainage and imbibitions processes in nanopores

There are two main pore-filling mechanisms in two-phase flow: drainage and imbibition. Drainage process refers to the situation where the non-wetting phase displaces

the wetting; this can only occur under the application of an external force. The opposite sequence, where the wetting phase displaces the non-wetting phase, is referred to as imbibitions process. It can occur spontaneously due to capillary forces or under the application of the external force. These two mechanisms are affected by pore sizes and morphology, fluids and solid properties (such as surface tension and viscosity), and boundary conditions.

Before every set of experiments, preliminary tests were conducted with the nanofluidic chip; no leakage was observed, and the flow was stable. The test section was cleaned by 0.1mole/L HCl, methanol and de-ionized water prior to use. All experiments were conducted at room temperature.

For the drainage process (gas displacing water), the nanopores were first 100% saturated with water (the wetting phase) by forced imbibition into the pre-vacuumed nanofluidic chip; then nitrogen gas (the non-wetting phase) was pressure-injected into the nanopores to displace water. The images of fluids flow during the displacements were recorded with the time interval of 100ms. As the water saturation decrease, the capillary pressure continuously increased. At each capillary pressure, the equilibrated water/gas ratio was obtained from analyzing the images. After the water/gas ratio in nanopores remained constant with the increase of gas pressure, the drainage process is considered as finished.

For the imbibitions process (water displacing gas), the nanopores were first saturated with nitrogen gas by pressure injection. Water was then injected into one of the microchannel while gas phase were continuously pressure injected into the other microchannel as the back pressure. By carefully reducing of gas injection pressure, water

started to invade into the nanopores and the imbibition processes started. The capillary pressure of the imbibitions process is considered as the same of the gas phase back pressure.

2.5 Measurement of relative permeability

Relative permeabilities of gas/water are measured by unsteady-state method based on the images of imbibition/drainage processes. Water relative permeability was measured from the drainage process. During gas displacing water, with controlled gas pressure, the water saturation in the nanopores kept decreasing until the capillary pressure reach to same as the gas phase external pressure. Thus the flow rate of water can be determined from the disappeared volume of water saturation in the nanopores versus time and the effective and relative water permeability can be calculated by using Darcy's law.

Gas relative permeability can be obtained from the imbibitions process, where gas saturation decreased until the capillary pressure decreased to same as the gas phase back pressure. Based on the disappeared volume of gas saturation in nanopores, the gas relative permeability was calculated based on Darcy's law.

3 RESULTS AND DISCUSSION

3.1 Mechanisms during drainage

The flow pattern and the interfaces of the water/gas during imbibitions/drainage processes were characterized from the images and the displacement mechanisms were discussed. The effects of nanopores dimensions and pore structures on the flow mechanisms were also investigated.

Displacement mechanism during drainage in parallel straight nanopores seems to be simple since piston-type motion occurred in most cases, as it showed in Figure 2. However, under relatively low capillary number, a distinctive pattern −"annular flow" was found for the drainage process in 100nm deep nanopores. This phenomenon has also been reported by our previous published work [88]. As it is showed in Figure 3, gas core filled the center of the nanochannels, surrounded by a water layer on the side walls. Similar flow pattern was reported in the multi-phase flow in conventional sized tubes [90, 91].
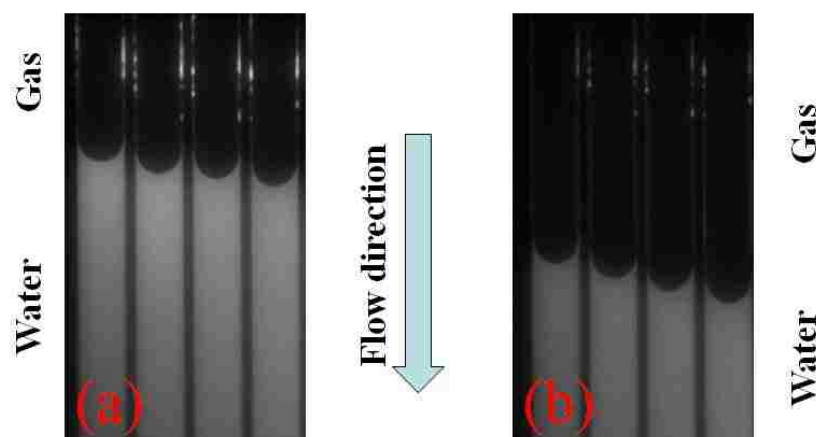

Figure 2. Piston-type motion of drainage process in 500nm deep nanopores.
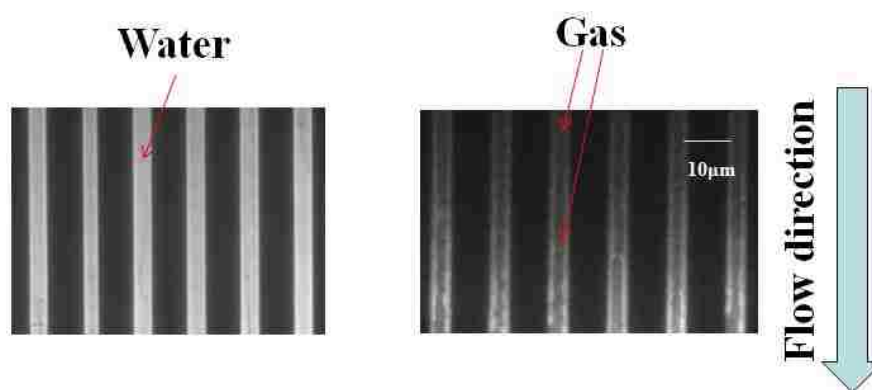
Figure 3. Annular-type flow of drainage process in 100nm deep nanopores.

For random network nanopores, Haines jump was found to be the major displacement mechanism. As it was described first by Haines [93], the Haines jump normally occurs when a interface passes through one pore to the other. When the non-wetting phase enters the pore from the pore throat, the velocity of the interface is normally slowed down due to the local entry capillary pressure. When the non-wetting phase comes out from a pore to the pore throat, the pressure of non-wetting phase is relatively high and the filling of the pore throat is faster. So the Haines jump is the phenomenon that the interfaces of two immiscible fluids appear to jump from one pore throat to the other pore throat during the drainage process. In our experiments, the Haines jumps were clearly observed and it was found that the jump could also split into multiple pores, as showed in Figure 4.
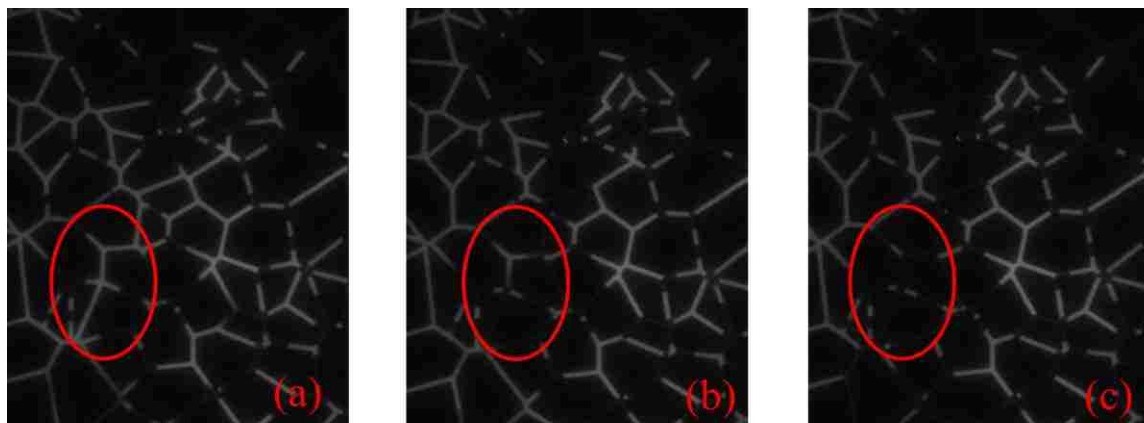
Figure 4. Haines jumps for drainage process in 300nm deep network nanopores.

3.2 Mechanisms during imbibitions

Piston-type motion and snap-off are two mechanisms are mostly reported in the imbibition process. Piston-type motion happened for the immiscible two phase imbibitions in the single tube. And the snap-off occurs at the pore throat where the non-wetting phase gets disconnected within a pore by the local invading of wetting phase into the pore throat. From the experimental results, it was found that the imbibitions mechanisms are more dependent on the pore structure than the nanopores dimensions.

For the parallel straight nanopores, piston-type motion appeared to be the most common displacement mechanisms, especially for the 500nm deep nanopores, as shown in Figure 5. This is easy to understand since there is no connection throat between each nanopore.
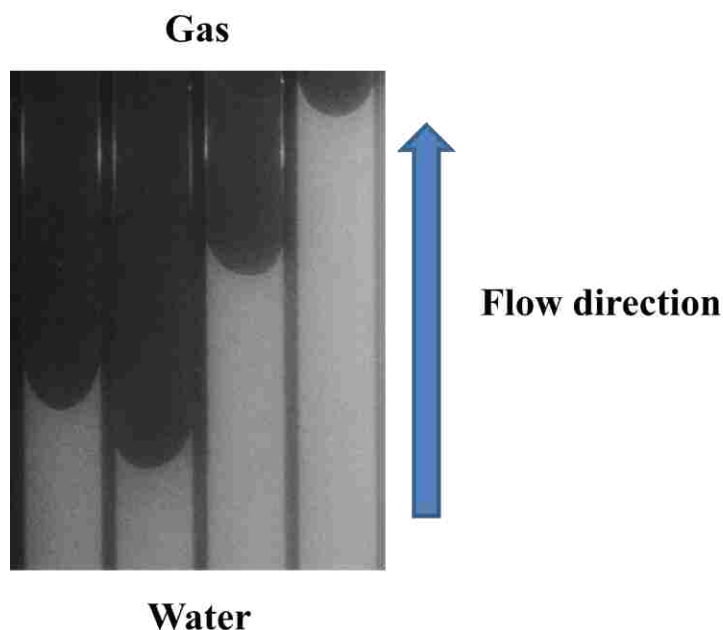
Figure 5. Piston-type motion for imbibition process in 500nm deep nanopores.

However, some other mechanism was observed. The images of the flow pattern are illustrated in Figure 6. Figure 6 shows parts of sequential images taken from the imbibition process in 500nm deep nanopores. The time interval between each picture was in 2 seconds. From image (a) to (f), the nanopores have been invaded by water. However, the displacement pattern was not piston-like meniscus. The water invasion presented in Figure 6 are only taking partial of the nanopores, where gas phase was disconnected as some "isolated islands" in the nanopores. This type of flow mechanisms can be considered as a type of local "snap-off". It is noticed that this type of displacement mechanism only appeared at low pressure and low capillary numbers. This mechanism

can be explained by the surface energy of gas/water interfaces. As it is proposed by Hassanizadeh and Gray [94], the capillary pressure can be expressed as the Gibbs free energy of the interfaces. It is known that liquids are intended to keep a spherical surface to minimum the surface energy. However the nanopores in the experiment had a high aspect ratio (width/depth = 50). Under such high aspect ratio, the surface energy of water/gas interfaces will be high to keep a piston-type motion. When the capillary pressure is lower than the surface energy required to keep the piston-type motion, the frontal water/gas surface area will reduce and thus the local "snap-off" mechanisms taken places.
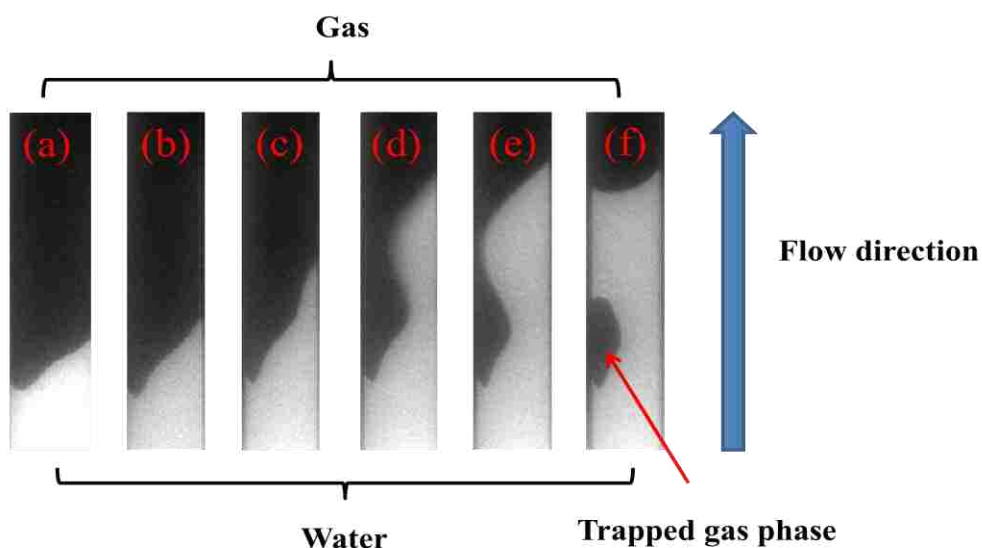
Figure 6. Local "snap-off" for imbibition process in 500nm deep nanopores.

For random network nanopores, piston-type motion were monitored in the single pore while snap-off happened at the pore throat. As it is shown in Figure 7, gas phase was trapped in the nanopores by invaded water and formed disconnected clusters, which was the residue gas.
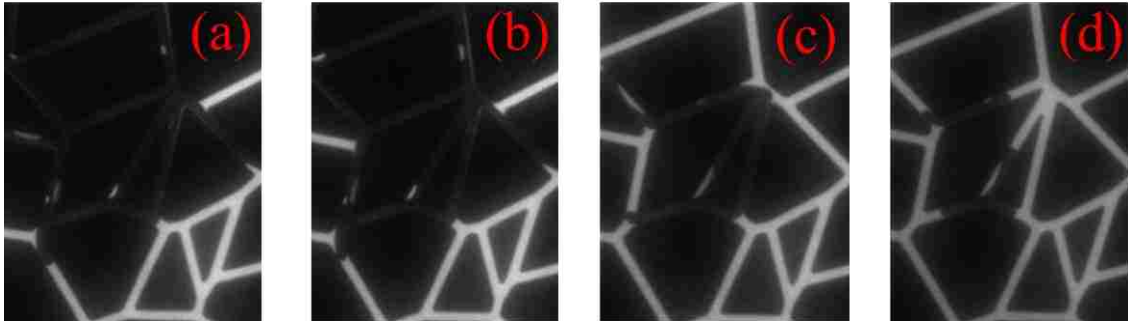
Figure 7. Snap-off for imbibition process in 300nm deep network nanopores.

Overall the snap-off mechanism was dominant in the imbibitions process, and the gas residue saturation is low. This is possibly due to the dimensions of pores pore throats. According to Wardlaw et al., [95] and Ioannidis et al., [96] when the pore size is similar to the pore throat, "cooperative filling" occurs more often than the snap-off where the wetting phase invasion increases significantly, as showed in Figure 8.
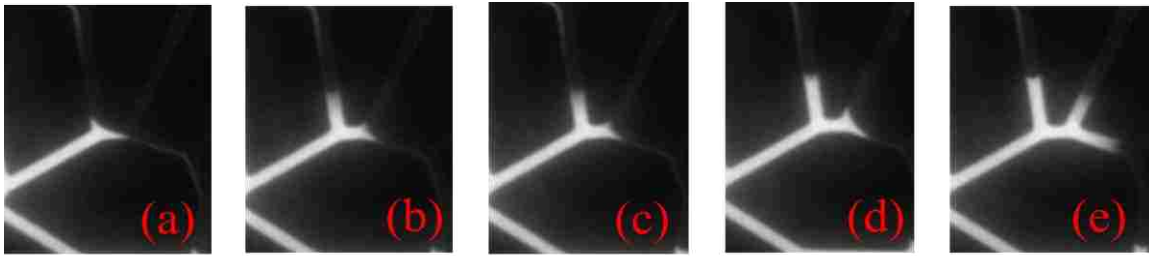
Figure 8. Cooperative filling for imbibition process in 300nm deep network nanopores.

3.3 Determination of capillary pressure vs. saturation

Capillary pressure is defined as the pressure difference between non-wetting phase and wetting phase. For two-phase flow in porous media, experimental results have proved that the capillary pressure is a function of fluid saturation.

As it is described in the experimental section, the relationship between capillary pressure and phase saturation in nanopores were investigated. Water saturations at various capillary pressures were calculated based on the percentage of water in the 2D image, which the saturation distribution along the Z-depth is assumed to be the same. The results of correlation between capillary pressure and phase saturation in the nanopores were showed in Figure 9 to Figure 11. For Figure 9, in the 500nm deep nanopores, the capillary pressure − saturation curves for drainage and imbibition processes are almost overlap to each other. The result indicates that the gas residue saturation in 500nm deep nanopores is very low so the effect on the drainage process can be negligible. And this assumption is agreed with the measured gas residue saturation (less than 2%).

Figure 10 showed the correlation between capillary pressure and phase saturation in the 300nm deep network nanopores. Compared with results in 500nm deep straight nanopores, there is a gap between the drainage and imbibition Pc-S curves and the slope of the curve is smaller (less flat). When the nanopores depth decreased to 100nm in Figure 11, the drainage and imbibition Pc-S curves are similar as the one obtained from the 500nm deep nanopores, with increased entrance pressure and irreducible water saturation.

Based on the results, the patterns of P_c-S curve didn't show a clear correlation with the change of pore sizes. It seems that the capillary pressure – saturation curves are also dependent on pore structure and saturation distribution. Similar P_c-S curve patterns were obtained for 500nm deep and 100nm deep nanopores with the similar parallel straight structure. Hassanizadeh and Gray [94] modified the theory of the relationship between capillary pressure and saturation by introduce the interfacial area. They proposed that the specific interfacial area between two-phases should be accounted as a variable in two-phase flow and determination of capillary pressures.

From our experimental results, in 500nm and 100nm deep parallel straight nanopores, the interfacial area between water and gas almost retained the same since piston-type motion domains in most cases. Thus, similar Pc-S curves were obtained with a relative flat pattern.
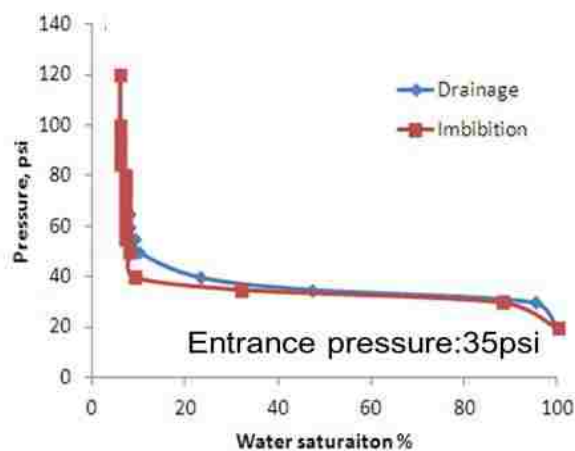
Figure 9. Relationship between capillary pressure and water saturation for drainage and imbibitions processes in 500nm deep nanochannels.
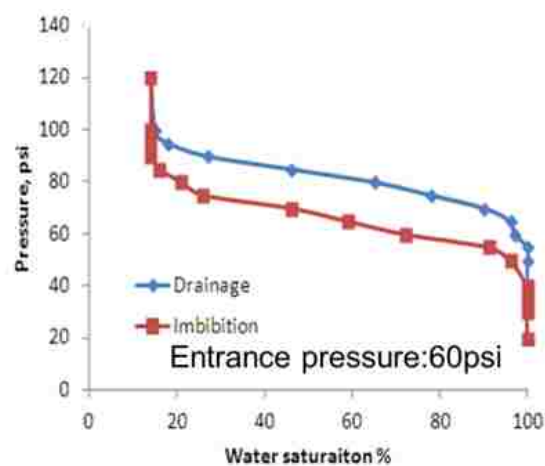
Figure 10. Relationship between capillary pressure and water saturation for drainage and imbibitions processes in 300nm deep network nanochannels.
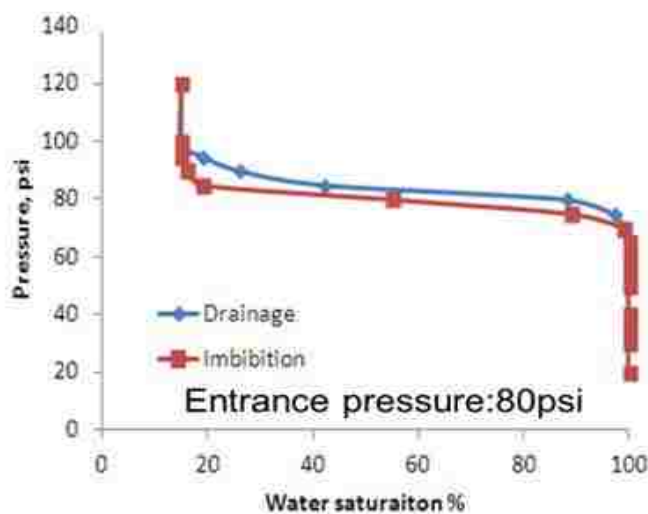
Figure 11. Relationship between capillary pressure and water saturation for drainage and imbibitions processes in 100nm deep nanochannels.

3.4 Determination of water/gas relative permeabilityin nano-scale porous media

The relative permeabilities of water/gas two phases as a function of saturation were measured as the method described in the experimental section.

Figure 12 shows the procedure of measuring water relative permeability in 500nm deep nanopores. From Figure 12 (a) to (f), sequential pictures were taken during the drainage process. The time interval between each picture is 20 seconds. At Figure 12 (a), the nanopores were mostly filled with water and the gas injection pressure was applied to displace water. From Figure 12 (b) to 12 (f), the water saturation in nanopores continuously decreased until the capillary pressure equaled with the gas injection pressure. As the water saturation decrease, the displacement rate slowed down. From the displacement rate and the applied pressure, the water relative permeability as a function

of water saturation can be obtained. The gas relative permeability was measured by the same principle from imbibitions process. The relationship between water/gas relative permeabilities and water saturation was summarized in Figure 13.

Figure 12. Measurement of water relative permeability from drainage process in 500nm deep nanopores. (a)~(f) are images of nanopores at different time with interval of 20 seconds.

From Figure 13, it is noticed that the relative permeabilities of water and gas were both measured before the breakthrough thus the flow is considered as unsteady state flow. This is mainly due to that the dimensions of the test section (nanopores) are extremely small and the drainage/imbibition would finish before reach to steady-state flow. For 500nm deep nanopores, the lowest wetting phase saturation (irreducible water saturation) that could be obtained during drainage was close to 6%, while the highest water phase

saturation obtained from imbibition as around 98%, indicates that the irreducible gas saturation in the 500nm deep nanopores is close to 2%. Both irreducible water and gas saturations are very low since the piston-type motion mechanism occurred in most cases, which yielded high displacement efficiency.

Figure 13. Relative permeability of the wetting and non-wetting phase with respect of wetting phase saturation in 500nm deep nanopores.

Figure 14 shows the procedure of measuring water relative permeability in 300nm deep network nanopores. From Figure 14 (a) to (f), sequential pictures were taken during the drainage process. The time interval between each picture is 60 seconds. The relationship between water/gas relative permeabilities and water saturation was summarized in Figure 15. In 300nm deep network nanopores, the breakthrough of either wetting phase or non-wetting phase occurred in the early stage of displacements. After

the breakthrough, the saturation of displaced phase continuously decreased until reach to irreducible saturation. And the relative permeability as a function of saturation was measured after the breakthrough. During drainage, the gas phase pressure progressively increased in order to overcome the entrance pressure and invade into the nanopores. As the gas phase reached the outlet of the nanopores, which is the breakthrough, the resistant pressure will suddenly drop since the micropores have much larger space. This means the gas phase pressure will be dropped and the displacement rate will be decreased.

In our experiments, the water saturation was around 70% at the breakthrough and the displacement rate was reduced right after the breakthrough. The irreducible water saturation in 300nm deep nanopores is close to 15%, while the irreducible gas saturation is around 12%.
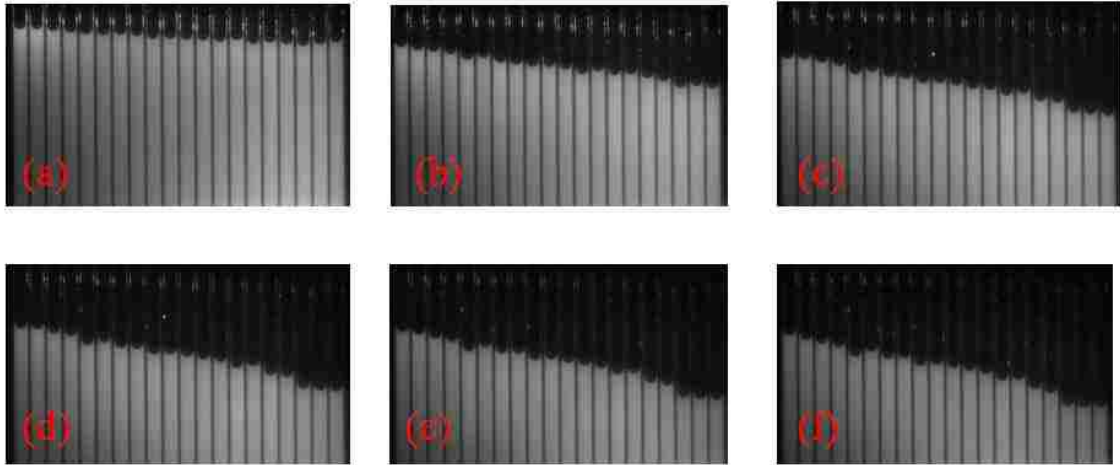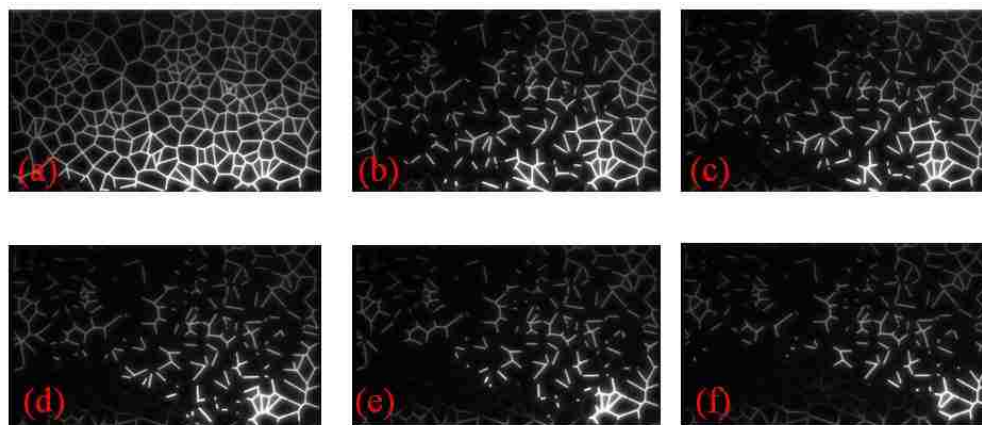

Figure 14. Measurement of water relative permeability from drainage process in 300nm deep network nanopores. (a)~(f) are images of nanopores at different time with interval of 60 seconds.
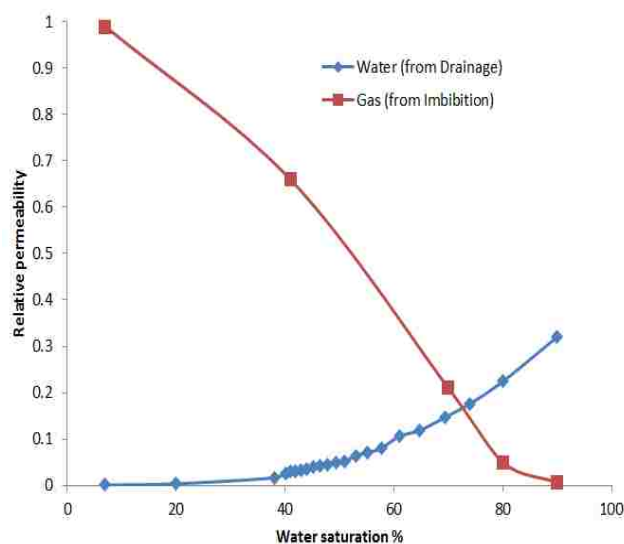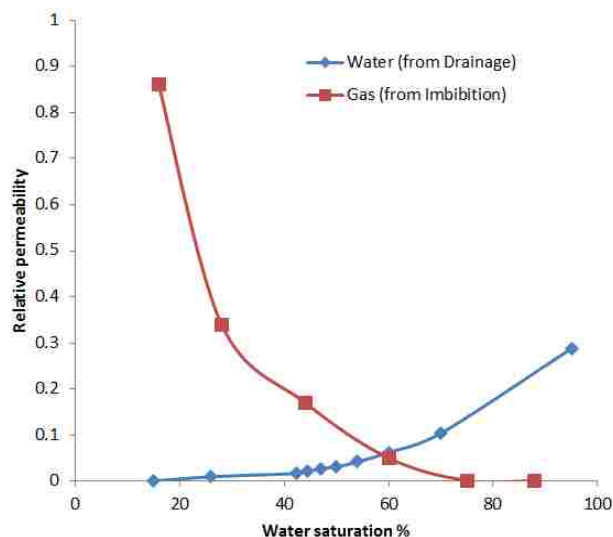
Figure 15. Relative permeability of the wetting and non-wetting phase with respect of wetting phase saturation in 300nm deep network nanopores.

4. CONCLUSIONS

In this work, a novel optic imaging method has been applied to measure the water/gas two phase displacements in nanopores. The displacement of two-phase in nanopores has been directly visualized and recorded as a function of time. The displacement mechanisms were first discussed as some distinctive mechanisms were found in both imbibitions and drainage processes. The relationship between capillary pressure and phase saturation for the nanopores with various dimensions and pore structures is reported for the first time. It was found that the capillary pressure is not only dependent on the phase saturation, but also largely dependent on the pore structure and specific interfacial area. Meanwhile, an unsteady-state method has been demonstrated to measure the relative permeability of water/gas in nanopores. This is also the first time to present the measurement of relative permeability as a function of wetting phase saturation

in nanopores. The experimental results obtained in this work could be very crucial for understanding the fluid flow behavior for unconventional resources and the developed method for capillary pressure and relative permeability measurement can be used for further studies and applications.

SECTION

2. CONCLUSIONS

In this work, a novel lab-on-chip approach for direct visualization of the water/gas flow behavior in nano-scale channels was developed by combining epi-fluorescence microscopy method with the nano-fluidic chip.

Water/gas single phase pressure driven flow was first studied. The single phase flow rate was determined by the developed concentration dependent fluorescence signal method. The linearity correlation between water flow rate and pressure drop in nano-scale channels was obtained and fit closely into the Poiseuille's Law. The results suggest that for 100nm deep nanochannels, the single phase water flow still follow the classic hydrodynamic flow model. Water/gas two-phase flow regime map for 100nm deep nano-scale channels was presented and compared with results in micro-scale channels. It was found that the two-phase flow patterns in nanochannels are essentially different from those of two-phase flows encountered in ordinary scale channels. No segmented flow was observed in nanochannels, possibly due to the large aspect ratio of the nanochannels.

The study of two-phase gas slippage indicates that under experimental conditions, the gas slippage factor increased as the water saturation increased. The possible flow mechanisms were proposed and proved by the flow pattern images. The displacements of water/gas two-phase flow nano-scale slit-like channels with various depths were investigated. The displacement mechanisms were first discussed as some distinctive

mechanisms were found in both imbibitions and drainage processes. The relationships between capillary pressure and phase saturation for the nanopores with various dimensions and pore structures were reported. It was found that the capillary pressure is not only dependent on the phase saturation, but also strongly correlated to on the pore structures and specific interfacial area. Meanwhile, an unsteady-state method was developed to measure the relative permeability of water/gas in nanopores. This is also the first time to present the measurement of relative permeability as a function of wetting phase saturation in nanopores.

The results of this work are crucial for permeability measurement and understanding fluid flow behavior for unconventional shale gas systems with nanopores.

BIBLIOGRAPHY

1. Cipolla, C.L., E. Lolon, and M.J. Mayerhofer. Reservoir modeling and production evaluation in shale-gas reservoirs. in *International Petroleum Technology Conference*. 2009. International Petroleum Technology Conference.

2. Gupta, D. Unconventional Fracturing Fluids for Tight Gas Reservoirs. in *SPE Hydraulic Fracturing Technology Conference*. 2009. Society of Petroleum Engineers.

3. Klinkenberg, L. The permeability of porous media to liquids and gases. *Drilling and production practice*, 1941.

4. Avraam, D. and A. Payatakes. Flow mechanisms, relative permeabilities, and coupling effects in steady-state two-phase flow through porous media. The case of strong wettability. *Industrial & engineering chemistry research*, 1999. 38(3): p. 778-786.

5. Baouab, Z., Najjari, M., Ouerfelli, H., & Nasrallah, S. B. Experimental study of the effects of hydraulic gradient and injected-gas flow rate on fragmentation in porous media. *Journal of Petroleum Science and Engineering*, 2007. 59(3): p. 250-256.

6. Budwig, R. Refractive index matching methods for liquid flow investigations. *Experiments in fluids*, 1994. 17(5): p. 350-355.

7. Chang, L. C., Tsai, J. P., Shan, H. Y., & Chen, H. H. Experimental study on imbibition displacement mechanisms of two-phase fluid using micro model. *Environmental Earth Sciences*, 2009. 59(4): p. 901-911.

8. Chen, J.-D. and D. Wilkinson. Pore-scale viscous fingering in porous media. *Physical review letters*, 1985. 55(18): p. 1892.

9. CoŞkuner, G. Microvisual study of multiphase gas condensate flow in porous media. *Transport in Porous Media*, 1997. 28(1): p. 1-18.

10.   Cottin, C., H. Bodiguel, and A. Colin. Influence of wetting conditions on drainage in porous media: A microfluidic study. *Physical Review E*, 2011. 84(2): p. 026311.

11.   Feng, Q. X., Di, L. C., Tang, G. Q., Chen, Z. Y., Wang, X. L., & Zou, J. X. *A visual micro-model study: The mechanism of water alternative gas displacement in porous media*. in *SPE/DOE Symposium on Improved Oil Recovery*. 2004. Society of Petroleum Engineers.

12.   Hatiboglu, C.U. and T. Babadagli. Pore-scale studies of spontaneous imbibition into oil-saturated porous media. *Physical Review E*, 2008. 77(6): p. 066311.

13.   Karadimitriou, N. K., Joekar-Niasar, V., Hassanizadeh, S. M., Kleingeld, P. J., & Pyrak-Nolte, L. J. A novel deep reactive ion etched (DRIE) glass micro-model for two-phase flow experiments. *Lab on a Chip*, 2012. 12(18): p. 3413-3418.

14.   Lenormand, R., C. Zarcone, and A. Sarr. Mechanisms of the displacement of one fluid by another in a network of capillary ducts. *Journal of Fluid Mechanics*, 1983. 135: p. 337-353.

15.   Theodoropoulou, M. A., Sygouni, V., Karoutsos, V., & Tsakiroglou, C. D. Relative permeability and capillary pressure functions of porous media as related to the displacement growth pattern. *International journal of multiphase flow*, 2005. 31(10): p. 1155-1180.

16.   Tsakiroglou, C. and D. Avraam. Fabrication of a new class of porous media models for visualization studies of multiphase flow processes. *Journal of materials science*, 2002. 37(2): p. 353-363.

17.   Tsakiroglou, C., D. Avraam, and A. Payatakes. Transient and steady-state relative permeabilities from two-phase flow experiments in planar pore networks. *Advances in water resources*, 2007. 30(9): p. 1981-1992.

18.   Tsakiroglou, C. D., Theodoropoulou, M., Karoutsos, V., Papanicolaou, D., & Sygouni, V. Experimental study of the immiscible displacement of shear-thinning fluids in pore networks. *Journal of colloid and interface science*, 2003. 267(1): p. 217-232.

19.   Wan, J., Tokunaga, T. K., Tsang, C. F., & Bodvarsson, G. S. Improved glass micromodel methods for studies of flow and transport in fractured porous media. *Water resources research*, 1996. 32(7): p. 1955-1964.

20.   Zhang, C., Oostrom, M., Wietsma, T. W., Grate, J. W., & Warner, M. G. Influence of viscous and capillary forces on immiscible fluid displacement: Pore-scale experimental study in a water-wet micromodel demonstrating viscous and capillary fingering. *Energy & Fuels*, 2011. 25(8): p. 3493-3505.

21.   Dawe, R.A., A. Caruana, and C.A. Grattoni. Immiscible displacement in cross-bedded heterogeneous porous media. *Transport in Porous Media*, 2011. 87(1): p. 335-353.

22.   Gunda, N. S. K., Bera, B., Karadimitriou, N. K., Mitra, S. K., & Hassanizadeh, S. M. Reservoir-on-a-Chip (ROC): A new paradigm in reservoir engineering. *Lab on a Chip*, 2011. 11(22): p. 3785-3792.

23.   Berejnov, V., N. Djilali, and D. Sinton. Lab-on-chip methodologies for the study of transport in porous media: energy applications. *Lab on a Chip*, 2008. 8(5): p. 689-693.

24.   Sohrabi, M., Tehrani, D. H., Danesh, A., & Henderson, G. D. Visualization of oil recovery by water-alternating-gas injection using high-pressure micromodels. *SPE Journal*, 2004. 9(03): p. 290-301.

25.   Cheng, J.T. and N. Giordano. Fluid flow through nanometer-scale channels. *Physical Review E*, 2002. 65: p. 031206.

26.   Cooper, S. M., Chuang, H. F., Cinke, M., Cruden, B. A., & Meyyappan, M. Gas permeability of a buckypaper membrane. *Nano Letters*, 2003. 3(2): p. 189-192.

27.   Han, A., Mondin, G., Hegelbach, N. G., de Rooij, N. F., & Staufer, U. Filling kinetics of liquids in nanochannels as narrow as 27 nm by capillary force. *Journal of Colloid and Interface Science*, 2006. 293: p. 151-157.

28.   Haneveld, J., Jansen, H. V., Tas, N. R., & Elwenspoek, M. C. Capillary filling of sub-10 nm nanochannels. *JOURNAL OF APPLIED PHYSICS*, 2008. 104: p. 014309.

29. Hibara, A., Saito, T., Kim, H. B., Tokeshi, M., Ooi, T., Nakao, M., & Kitamori, T. Nanochannels on a Fused-Silica Microchip and Liquid Properties Investigation by Time-Resolved Fluorescence Measurements. *Anal. Chem*, 2002. 74(24): p. 6170-6176.

30. Holt, J. K., Park, H. G., Wang, Y., Stadermann, M., Artyukhin, A. B., Grigoropoulos, C. P., Bakajin, O. Fast mass transport through sub-2-nanometer carbon nanotubes. *Science*, 2006. 312(5776): p. 1034-1037.

31. Lysenko, V., Vitiello, J., Remaki, B., & Barbier, D. Gas permeability of porous silicon nanostructures. *Physical Review E*, 2004. 70(1): p. 017301.

32. Mao, P. and J. Han. Fabrication and characterization of 20 nm planar nanofluidic channels by glass–glass and glass–silicon bonding. *Lab on a Chip*, 2005. 5(5): p. 837-844.

33. Phan, V. N., Nguyen, N. T., Yang, C., Joseph, P., Djeghlaf, L., Bourrier, D., & Gue, A. M. Capillary Filling in Closed End Nanochannels. *Langmuir*, 2010. 26: p. 13251-13255.

34. Tamaki, E., Hibara, A., Kim, H. B., Tokeshi, M., & Kitamori, T. Pressure-driven flow control system for nanofluidic chemical process. *Journal of Chromatography A*, 2006. 1137: p. 256-262.

35. Tas, N. R., Escalante, M., van Honschoten, J. W., Jansen, H. V., & Elwenspoek, M. Capillary Negative Pressure Measured by Nanochannel Collapse. *Langmuir*, 2010. 26(3): p. 1473-1476.

36. Tas, N. R., Haneveld, J., Jansen, H. V., Elwenspoek, M., & Van Den Berg, A. Capillary filling speed of water in nanochannels. *APPLIED PHYSICS LETTERS*, 2004. 85(15): p. 3274-3276.

37. Verweij, H., M.C. Schillo, and J. Li. Fast mass transport through carbon nanotube membranes. *Small*, 2007. 3(12): p. 1996-2004.

38. Whitby, M. and N. Quirke. Fluid flow in carbon nanotubes and nanopipes. *Nature Nanotechnology*, 2007. 2(2): p. 87-94.

39.   Neeves, K. B., Lo, C. T., Foley, C. P., Saltzman, W. M., & Olbricht, W. L. Fabrication and characterization of microfluidic probes for convection enhanced drug delivery. *J. Controlled Release*, 2006. 111(3): p. 252-262.

40.   Chung, A.J., D. Kim, and D. Erickson. Electrokinetic microfluidic devices for rapid, low power drug delivery in autonomous microsystems. *Lab on a Chip*, 2008. 8(2): p. 330-338.

41.   Shestopalov, I., J.D. Tice, and R.F. Ismagilov. Multi-step synthesis of nanoparticles performed on millisecond time scale in amicrofluidic droplet-based system. *Lab on a Chip*, 2004. 4: p. 316-321.

42.   Kaban'kov, O.N. and A.P. Sevast'yanov. Two-phase flows: a review. *Heat Transfer Res*, 2000. 31: p. 103-122.

43.   Berejnov, V., N. Djilali, and D. Sinton. Lab-on-chip methodologies for the study of transport in porous media: energy applications. *Lab on a Chip*, 2008. 8: p. 689-683.

44.   Hibiki, T. and K. Mishima. Flow regime transition criteria for upward two-phase flow in vertical narrow rectangular channels. *Nuclear Engineering and Design*, 2001. 203: p. 117-131.

45.   Phan, V.-N., C. Yang, and N.-T. Nguyen. Analysis of capillary filling in nanochannels with electroviscous effects. *Microfluid Nanofluid*, 2009. 7: p. 519-230.

46.   Chen, X. Y., Toh, K. C., Chai, J. C., & Yang, C. Developing pressure-driven liquid flow in microchannels under the electrokinetic effect. *International Journal of Engineering Science*, 2004. 42: p. 609-622.

47.   Dutta, D., A. Ramachandran, and D.T.L. Jr. Effect of channel geometry on solute dispersion in pressure-driven microfluidic systems. *Microfluid Nanofluid*, 2006. 2: p. 275-290.

48.   Lauga, E. and H.A. Stone. Effective slip in pressure-driven Stokes flow. *J. Fluid Mech*, 2003. 489: p. 55-77.

49.   Ward, T., Faivre, M., Abkarian, M., & Stone, H. A. Microfluidic flow focusing: Drop size and scaling in pressure versus flow-rate-driven pumping. *Electrophoresis*, 2005. 26: p. 3716-3724.

50.   Raghu, R.C. and J. Schofield. Simulation of Pressure-Driven Flows in Nanochannels Using Multiparticle Collision Dynamics. *J. Phys. Chem. C*, 2010. 114: p. 20659-20671.

51.   Serizawa, A., Z. Feng, and Z. Kawara. Two-phase flow in microchannels. *Experimental Thermal and Fluid Science* 2002. 26: p. 703-714.

52.   Mandhane, J.M., G.A. Gregory, and K. Aziz. A flow pattern map for gas–liquid flow in horizontal pipes. *Int. J. Multiphase Flow*, 1974. 1(4): p. 537-553.

53.   Travis, K.P., B.D. Todd, and D.J. Evans. Departure from Navier-Stokes hydrodynamics in confined liquids. *Physical Review E*, 1997. 55(4): p. 4288-4295.

54.   Cuenca, A. and H. Bodiguel. Fluorescence photobleaching to evaluate flow velocity and hydrodynamic dispersion in nanoslits. *Lab on a Chip*, 2012. 12: p. 1672-1679.

55.   Sinton, D. Microscale flow visualization. *Microfluidic And Nanofluidic*, 2004. 1(1): p. 2-21.

56.   Gai, H., Li, Y., Silber-Li, Z., Ma, Y., & Lin, B. Simultaneous measurements of the flow velocities in a microchannel by wide/evanescent field illuminations with particle/single molecules. *Lab on a Chip*, 2005. 5(5): p. 443-449.

57.   Gai, H., Wang, Q., Ma, Y., & Lin, B. Correlations between Molecular Numbers and Molecular Masses in an Evanescent Field and Their Applications in Probing Molecular Interactions. *Angewandte Chemie*, 2005. 117(32): p. 5237-5240.

58.   Banerjee, A., Shuai, Y., Dixit, R., Papautsky, I., & Klotzkin, D. Concentration dependence of fluorescence signal in a microfluidic fluorescence detector. *Journal of Luminescence*, 2010. 130: p. 1095-1100.

59.   Penzkofer, A. and W. Leupacher. S0-S1 two photon absorption dynamics of organic dye solutions. *Optical and Quantum Electronic*, 1987. 19(6): p. 327-349.

60.   Bindhu, C. V., Harilal, S. S., Varier, G. K., Issac, R. C., Nampoori, V. P. N., & Vallabhan, C. P. G. Measurement of the absolute fluorescence quantum yield of rhodamine B solution using a dual-beam thermal lens technique. *Journal of Physics D: Applied Physics*, 1996. 29(4): p. 1074-109.

61.   Qi, D., D.J. Hoelzle, and A.C. Rowat. Probing single cells using flow in microfluidic devices. *The European Physical Journal*, 2012. 204: p. 85-101.

62.   Elazhary, A.M. and H.M. Soliman. Two-phase flow in a horizontal mini-size impacting T-junction with a rectangular cross-section. *International Journal of Multiphase Flow*, 2012. 42: p. 104-113.

63.   Yang, Z. C., Bi, Q. C., Liu, B., & Huang, K. X. Nitrogen/non-Newtonian fluid two-phase upward flow in non-circular microchannels. *International Journal of Multiphase Flow*, 2010. 36: p. 60-70.

64.   Kawahara, A., P.M.-Y. Chung, and M. Kawaji. Investigation of two-phase flow pattern, void fraction and pressure drop in a microchannel. *International Journal of Multiphase Flow*, 2002. 28: p. 1411-1435.

65.   Saisorn, S. and S. Wongwises. The effects of channel diameter on flow pattern, void fraction and pressure drop of two-phase air–water flow in circular micro-channels. *Experimental Thermal and Fluid Science*, 2010. 34: p. 454-462.

66.   Ide, H., A. Kariyasaki, and T. Fukano. Fundamental data on the gas-liquid twophase flow in Minichannels. *Int. J. Thermal Sci*, 2007. 46: p. 519-530.

67.   Rose, W.D. Permeability and gas-slippage phenomena. *28 th Annual Mtg. Topical Committee on Production Technology*, 1948.

68.   Javadpour, F. Nanopores and apparent permeability of gas flow in mudrocks (shales and siltstone). *Journal of Canadian Petroleum Technology*, 2009. 48(8): p. 16-21.

69.   Loosveldt, H., Z. Lafhaj, and F. Skoczylas. Experimental study of gas and liquid permeability of a mortar. *Cement and Concrete Research*, 2002. 32(9): p. 1357-1363.

70.   Jones, F.O. and W. Owens. A laboratory study of low-permeability gas sands. *Journal of Petroleum Technology*, 1980. 32(9): p. 1631-1640.

71.   Civan, F., C.S. Rai, and C.H. Sondergeld. Shale-gas permeability and diffusivity inferred by improved formulation of relevant retention and transport mechanisms. *Transport in Porous Media*, 2011. 86(3): p. 925-944.

72.   Xiong, X., Devegowda, D., Villazon, M., German, G., Sigal, R. F., & Civan, F. A Fully-Coupled Free and Adsorptive Phase Transport Model for Shale Gas Reservoirs Including Non-Darcy Flow Effects. in *SPE Annual Technical Conference and Exhibition*. 2012.

73.   Swami, V., C. Clarkson, and A. Settari. Non-Darcy Flow in Shale Nanopores: Do We Have a Final Answer? in *SPE Canadian Unconventional Resources Conference*. 2012.

74.   Javadpour, F., D. Fisher, and M. Unsworth. Nanoscale gas flow in shale gas sediments. *Journal of Canadian Petroleum Technology*, 2007. 46(10).

75.   Fulton, P.F. The effect of gas slippage on relative permeability measurements. *Producers Monthly*, 1951. 15(12): p. 14-19.

76.   Li, K. and R. Horne. Experimental study of gas slippage in two-phase flow. *SPE Reservoir Evaluation & Engineering*, 2004. 7(6): p. 409-415.

77.   Qingjie, L., Baohua, L., Xianbing, L., & Shouguo, Y. The effect of water saturation on gas slip factor by pore scale network modeling. in *SCA 2002 Symposium, Monterey, California, September*. 2002.

78.   Rushing, J., K. Newsham, and K. Fraassen. Measurement of the two-phase gas slippage phenomenon and its effect on gas relative permeability in tight gas sands. in *SPE Annual Technical Conference and Exhibition*. 2003.

79.   Sampath, K. and C. Keighin. Factors affecting gas slippage in tight sandstones of cretaceous age in the Uinta basin. *Journal of Petroleum Technology*, 1982. 34(11): p. 2715-2720.

80.   Wan, J. and J.L. Wilson. Visualization of the role of the gas-water interface on the fate and transport of colloids in porous media. *Water Resources Research*, 1994. 30(1): p. 11-24.

81.   Lanning, L.M. and R.M. Ford. Glass micromodel study of bacterial dispersion in spatially periodic porous networks. *Biotechnology and bioengineering*, 2002. 78(5): p. 556-566.

82.   Javadpour, F. and D. Fisher. Nanotechnology-based micromodels and new image analysis to study transport in porous media. *Journal of Canadian Petroleum Technology*, 2008. 47(2).

83.   Ikeda, M., Tang, G. Q., Ross, C., & Kovscek, A. Oil Recovery and Fracture Reconsolidation of Diatomaceous Reservoir Rock by Water Imbibition at High Temperature. in *SPE Annual Technical Conference and Exhibition*. 2007.

84.   Ross, C. M., Ikeda, M., Tang, G. Q., & Kovscek, A. R. Alteration of Reservoir Diatomites by Hot Water Injection. in *SPE Western Regional and Pacific Section AAPG Joint Meeting*. 2008.

85.   Ross, C. and A. Kovscek. Pore Microstructure and Fluid Distribution in a Diatomaceous Reservoir. in *SPE/DOE Improved Oil Recovery Symposium*. 2002.

86.   Buchgraber, M., Clemens, T., Castanier, L. M., & Kovscek, A. R. The displacement of viscous oil by associative polymer solutions. in *SPE Annual Technical Conference and Exhibition*. 2009.

87.   Funatsu, T., Harada, Y., Tokunaga, M., Saito, K., & Yanagida, T. Imaging of single fluorescent molecules and individual ATP turnovers by single myosin molecules in aqueous solution. *Nature*, 1995. 374(6522): p. 555-559.

88.   Wu, Q., Ok, J. T., Sun, Y., Retterer, S. T., Neeves, K. B., Yin, X., Bai, B., & Ma, Y. (2013). Optic imaging of single and two-phase pressure-driven flows in nano-scale channels. *Lab on a Chip*, *13*(6), 1165-1171.

89. Dullien, F.A.L. Porous media: fluid transport and pore structure. Vol. 2. 1992: Academic press San Diego.

90. Yue, J., Chen, G., Yuan, Q., Luo, L., & Gonthier, Y. Hydrodynamics and mass transfer characteristics in gas–liquid flow through a rectangular microchannel. *Chemical Engineering Science*, 2007. 62(7): p. 2096-2108.

91. Saisorn, S. and S. Wongwises. The effects of channel diameter on flow pattern, void fraction and pressure drop of two-phase air–water flow in circular micro-channels. *Experimental thermal and fluid science*, 2010. 34(4): p. 454-462.

92. Serizawa, A., Z. Feng, and Z. Kawara. Two-phase flow in microchannels. *Experimental Thermal and Fluid Science*, 2002. 26: p. 703-714.

93. Haines, W.B. Studies in the physical properties of soil. V. The hysteresis effect in capillary properties, and the modes of moisture distribution associated therewith. *The Journal of Agricultural Science*, 1930. 20(01): p. 97-116.

94. Hassanizadeh, S.M. and W.G. Gray. Thermodynamic basis of capillary pressure in porous media. *Water resources research*, 1993. 29(10): p. 3389-3405.

95. Wardlaw, N.C. and L. Yu. Fluid topology, pore size and aspect ratio during imbibition. *Transport in Porous Media*, 1988. 3(1): p. 17-34.

96. Ioannidis, M.A., I. Chatzis, and A.C. Payatakes. A mercury porosimeter for investigating capillary phenomena and microdisplacement mechanisms in capillary networks. *Journal of colloid and interface science*, 1991. 143(1): p. 22-36.

VITA

Qihua Wu was born in Henan province in China. He graduated with a Bachelor Degree in Chemistry from Xiamen University in Xiamen, Fujian province in China in 2009. He then attended Missouri University of Science and Technology (formerly the University of Missouri - Rolla) since August, 2009. His research focuses on imaging of fluid flow in lab-on-chip devices and environmental monitoring.